國 立 交 通 大 學
顯 示 科 技 研 究 所

碩 士 論 文

氮化鎵族奈米結構之光學特性

Optical Characteristics of Nitride-based Nanostructures

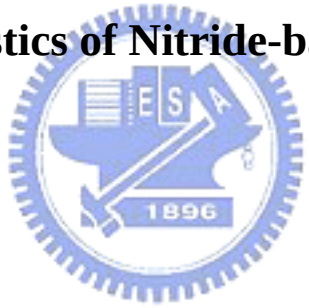

研究生 ： 游敏

指導教授 ： 郭浩中教授

中 華 民 國 九 十 五 年 七 月

氮化鎵族奈米結構之光學特性

Optical Characteristics of Nitride-based Nanostructures

研 究 生：游敏　　Student：Min Yu

指導教授：郭浩中　　Advisor：Prof. Hao-Chung Kuo

國 立 交 通 大 學

顯 示 科 技 研 究 所

碩 士 論 文

A Thesis

Submitted to Department of Photonics

Institute of Display

College of Electrical Engineering and Computer Science

National Chiao Tung University

in Partial Fulfillment of the Requirements

for the Degree of

Master

in

Display

July 2006

Hsinchu, Taiwan, Republic of China

中華民國九十五年七月

氮化鎵族奈米結構之光學特性

研究生 ： 游敏　　指導教授 ： 郭浩中教授

國立交通大學顯示科技研究所碩士班

摘要

本論文中，我們研究兩種以化學氣相沉積法成長的奈米結構樣品，前者為氮化銦鎵/氮化鎵量子點，後者為以 a 軸成長的氮化銦鎵/氮化鎵的多重量子井，我們利用光激發螢光(PL) ，螢光激發光(PLE)等光譜技術配合理論模擬進行光學特性的分析。

在第一部分我們利用一種新的成長方法長出高密度氮化鎵量子點之樣品，透過原子力顯微鏡的量測得知量子點的大小會隨著SiN_x處理時間的增加而變大，藉由光激發螢光光譜的分析顯示小量子點表現出較強的量子侷限效應，因此相較於大的量子點其波長較短，同時我們以模擬的方式計算量子侷限效應的理論值，和實驗大致吻合。再者我們將量子點的樣品做了熱退火的處理。我們觀察到隨著退火的溫度從 650 °C 增加至 950 °C時，量子點的光譜表現出先紅移再藍移的趨勢，且小的量子點相較於大的量子點紅移較多。針對這個結果我們也建立了一個物理模型以理論計算解釋成因。

第二部分我們以相同的長晶條件製備了兩組樣品，為以 a 軸和 c 軸成長的氮化銦鎵/氮化鎵多重量子井，實驗的結果顯示 a 軸樣品之內建電場不影響量子井的位能，我們期待可藉由此特性提高內部量子效率。除此之外，我們發現在 20k 的低溫下 a 軸樣品的光譜包含了兩個波峰。高能量的波峰在變溫的過程中表現出快速的熱抑制(thermal quenching)效應，而低能量的波峰維持至室溫。在螢光激發光 PLE 的實驗中我們也觀察到 a 軸樣品的史托克位移(stoke's shift)較大，藉由這兩個結果可得知銦含量在 a 軸樣品中較不均勻所以導致明顯的侷限效應(localization effect) 。在本論文的最後我們以側向成長的結構減少缺陷密度，改善了 a 軸樣品的品質。

Optical Characteristics of Nitride-based Nanostructures

Student : Min Yu Advisor : Prof. Hao-Chung Kuo

Institute of Display

National Chiao Tung University

Abstract

In this thesis, two kinds of nanostructures grown by metalorganic chemical vapor deposition have been investigated. First, the characteristics of InGaN/GaN quantum dots in different sizes were demonstrated. Second, the comparison of a-plane InGaN/GaN multiquantum wells grown on r-plane sapphire and c-plane samples were studied. We utilized photoluminescence (PL), photoluminescence excitation (PLE) system and simulation to investigate the optical properties of our samples.

In the first part, we investigate the optical and structural properties of ultra-high-density InGaN/GaN QDs with different sizes. Atomic force microscopy revealed the size of QDs witch was increased with the duration of SiN_x. Small QDs with larger quantum confine exhibited blue-shift on PL peak than the larger QDs. The emission energies are in agreement with the calculated transition energies. On the other hand, the thermal anneal effect were studied. When annealing temperature increased from 650 ˚C to 950 ˚C, a red-shift followed by a blue-shift on PL peaks emitted from InGaN/GaN QDs was observed. And we observed small QD exhibited large red shift than large quantum dot. Finally, we develop a model to explain the mechanism. It is proposed that the red-shift was dominated by size enlargement of QD. As further increasing the annealing time, the blue-shift of PL emission peaks was attributed to decrease of the QD potential depth caused by out-diffusion of the indium composition in QDs.

In the second part, a-plane and c-plane MQWs with the same growth condition were prepared to be compared in their optical characteristic. The presence of obvious power-depend blue-shift on PL peak was observed for c-plane MQWs, whereas less shift was observed for a-plane MQWs. The power dependent PL experiment indicated the polarization does not affect in the direction of well in a-plane InGaN/GaN MQWs. This characteristic could be introduced to enhance the internal quantum efficiency. Furthermore, we investigate the localization effect on a-plane InGaN MQW using temperature dependent PL and PLE Low temperature PL spectrum exhibited two dominant peaks in a-plane MQW. The apparent thermal quenching on high energy peak, whereas the luminance of low energy one maintain even until room temperature. And the lager stoke shift in a-plane MQW than c-plane MQW was addressed by PLE measurement. Those phenomenon demonstrated that the localization effect obviously appear in a-plane InGaN MQW. Finally, epitaxial lateral overgrowth (ELOG) method was used to reduce the defect density and also improve sample quality.

致謝

畢業在即，兩年來的碩士生活獲益良多，在這裡謝謝大家對我的照顧。

首先感謝王興宗教授對我的肯定，讓我這兩年的研究生活能夠不畏艱難，勇往直前；謝謝郭浩中教授對我的了解及分派適任的工作，並在困難時給予指引；也謝謝盧廷昌教授在論文上的指導，讓我順利完成研究；希望老師們一起齊力將實驗室帶向另一番榮景。

博士班的亞衡學長帶領我認識儀器的架設和實驗分析的技巧，也在做人處世上給予寶貴的意見，你一直是我進步的動力；謝謝敏瑛學姊的耐心教導，還有親切體貼的道鴻學長、芳儀學姊總不吝惜指教，你們豐富了我碩一的生活。謝謝德宗學長在上游把關，提供優質的樣品，和你一起研究討論非常開心。小賴學長，實驗不順利時更多虧有你的支持，在你身上我看到認真負責的典範，希望你在實驗室一切順利；宗憲學長，和你直來直往的討論很是過癮；多謝陳博 TEM 的支援及提供許多經驗談；姚忻宏學長，謝謝你的包容，一切盡在不言中；小朱學長，和你一起實驗很開心，叔叔果然是騙人的！小強學長，謝謝你在迷惘時給予適時的指點，你們兩位的幽默讓實驗室充滿寓教於樂的驚喜，繼續保持喔。

同學宗鼎常常幫大家計畫活動、擔當重任，你絕對會是一個優秀的領導人。剛帆，多虧你規劃了畢業旅行，讓大家留下難忘的回憶，常常要開車載大家真是辛苦你了。文凱，大家常常開你玩笑是因為你脾氣最好，從不動怒，但是瘦一點真的比較好看喔。志堯，你的細心加上美術天份再次強烈地印證你的綽號，不要再瞞我了喔。柏傑，看到你就想到肯德基的美味。皇申，用你的可愛及歌聲征服群創的工程師吧！最重要的，從大學就一起打拼的意偵，謝謝你長久以來的相伴，認識你這個朋友真是幸運。希望全體碩二的同學友誼長存，you are the best！

體貼的潤琪學妹幫我分擔了實驗，紓解我的壓力，能夠帶妳我覺得真是開心！認真敦厚的家樸學弟，雖然你比我早進實驗室做專題，不過真是不好意思，先走一步囉。直攻博士班的碩鈞，你是任重而道遠呀。苗條的金門，數代單傳的

重責大任就靠你啦。孟儒，希望有機會還能一起打球。網球之神卓毅，熱血青年瑞農，永遠 18 歲的乃方學姊，祝你們實驗順利。

感謝我多年的好友坤憲、貽婷、筑雅、鴨子給予精神上的支持，你們的友誼是我珍貴的收藏，最後謹把我的論文獻給我最愛的家人。

List of Tables

List of Figures

Chapter 1 Introduction

1.1 The characteristic of semiconductor nanostructure

Low dimension structure as the active layer was widely applied in these optical devices to operate in low threshold current, reduce temperature sensitivity and enhance the emitting efficiency due to quantum confine effect [1-2]. Because of the different dimensional confinement of carrier and density of state, the nanostructure can be classify into quantum well (QW), nanowire and quantum dot (QD) by their density of state as shown in Fig. 1.1.1. The bulk material has three dimensional density of state and the shape is parabolic function, the energy state of carrier is continues above energy band-gap. Then two dimensional structures, such as quantum well, is a step function due to one dimensional confinement of carrier. With decreasing the degree of freedom of carriers, the density of state of zero-dimensional structure, as quantum dot, manifest delta function density of state. As a result, the electronic states are quantized and the energy levels become discrete. In Figure 1.1.2, we could see the carriers are localized in the quantum dot structure of three dimensional confinements. There are some unique characteristics in the quantum dot structures. Discrete energy state is an attractive benefit applied to decrease the half of full width in emitting spectrum and separate the different quantum state level. The lasing behavior and quantum information analysis can be improved by their development. Recently, InGaN alloy is a potential material for the realized of visible light emitting diodes (LEDs) and laser diodes (LDs) [3-6]. For wurtzite structure, the band gap of GaN and InN are 3.4eV and 0.7eV. Raising the wavelength of In_xGaN_{1-x} can be adjusted ranging from ultraviolet to red by increasing In composition. In this thesis, InGaN based nanostructure was investigated.

1.2 The development of nonpolar structure

One of the unique characteristics of III-V nitride material is the presence of the build in field. The build in field is the combination of spontaneous polarization and the strain-induced polarization depending on the lattice mismatch. The build in field would result in potential bending witch called quantum confine stark effect (QCSE). This feature results in that carriers tend to situate in one side of the triangular potential wells. The overlap of electron and hole wave functions decrease with increasing the well width. In order to increase the internal quantum efficiency, the reduction of the polarization effect was an important issue. A useful approach to overcome this problem was the fabrication of the structure along non-polar direction. The bonding of Ga and N atom is along [1000] axis and orthogonal to the growth axis. As a result the internal build-in electric field doesn't influence quantum well along the growth direction. There are two ways for realization non-polar structure in common. The first approach is growing [1100] oriented m-plane GaN template on closely lattice matched [100] plane of $LiAlO_2$ by hydride vapor phase epitaxy (HVPE) and molecular beam epitaxy (MBE) [7]. The Second is growing $[11\bar{2}0]$ oriented a-plane GaN template on r-plane sapphire or $[11\bar{2}0]$ SiC by metalorganic vapor-phase (MOVPE) [7-8]. Hexagonal wurtzite structure of GaN was shown in figure 1.2.1 and different plane with orientation is illustrated. Nonpolar structure has been applied to grow AlGaN/GaN and InGaN/GaN heterostructures. To date, the characteristic of the nonpolar structure have been demonstrated in some reports [9-12] In InGaN QWs , the near band edge emission is related to nonradiative process and radiative process, in polar structure, nonradiative process is dominated by the electron-hole wavefunciton separation due to quantum-confined stark effect (QCSE). The radiative process is enhanced by the localization excitons due to the spatial In-rich cluster. In

this thsis, the polarization effect and localization behavior of a-plane InGaN MQWs are discussed.

1.3 Motivation

Nearly, compared with conventional quantum well (QW) structure, the fabrication of quantum dot (QD) with three dimensional confinements of carriers and delta-like function attract a lot of attention. In this thesis, the InGaN QD was grown by antisurfactant method. We investigated the structure and optical properties for different size QD and developed the simulation to study the energy transition. Moreover, we investigated the effect of thermal annealing for different size QD with a series annealing temperature. We also provide a theoretical simulation to analyze the mechanism of the InGaN/GaN QDs of thermal annealing.

Nonpolar structure is fabricated in order to increase the internal quantum efficiency. It is not affected by polarization effect based on the direction of Ga and N atoms arrange normal to the growth axis. In this thesis, a-plane and c-plane MQWs with the same growth condition were prepared to be compared in their optical characteristic.

Nonpolar *a*-plane GaN base material grown on *r*-plane sapphire substrates which\ always accompany with a wavy, stripe-like growth feature possess a large density of threading dislocations and stacking faults. It is result from serious aniostropic in-plane strain between different crystal axis [53]. Recently, successful epitaxial lateral overgrowth (ELOG) of *a*-plane GaN on *r*-plane sapphire has been reported. ELOG not only improves significantly the material quality by reducing the density of threading dislocations but also alleviates the strain-related surface roughening and faceting [54-55]. Despite the ELOG assisted morphology and quality improvements in *a*-plane GaN over *r*-plane sapphire, the study of the epilayer quality and dislocations distribution in the ELOG epilayer is quite not lucid. In this letter, we

successfully improve $[11\bar{2}0]$ *a*-plane GaN quality by using TELOG and the optical and structural properties is presented explicitly.

The organization of this thesis is as following: the analyses of nanostructure optical properties were investigated. In the chapter 2, we discuss the characteristic of InGaN based nanostructure, the simulation and growth methods of InGaN QD. The experiment principle and set up are described in the chapter 3. The detailed experimental results, theoretical analysis and the effects of thermal annealing for InGaN QD are presented in the chapter 4. In the chapter 5, we study the optical properties of a-plane InGaN/GaN MQW and compared with the behavior of c-plane samples. In the chapter 6, the TELOG was introduced to improve the sample quality. Finally, we give a conclusion of the thesis in the chapter 6.

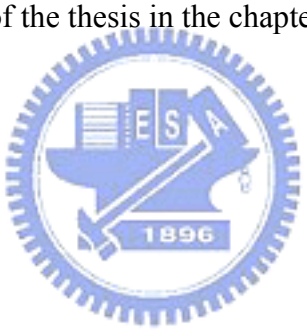

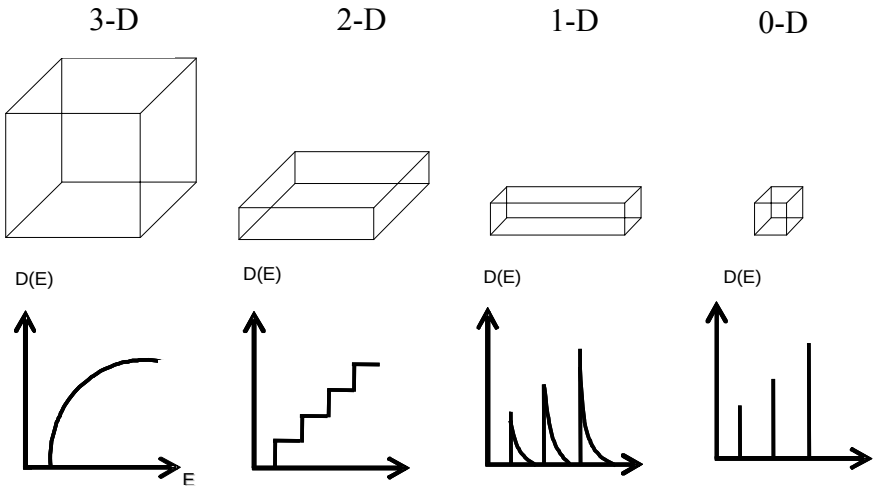

Fig 1.1.1 Dimension of nanostructure and corresponding density of state

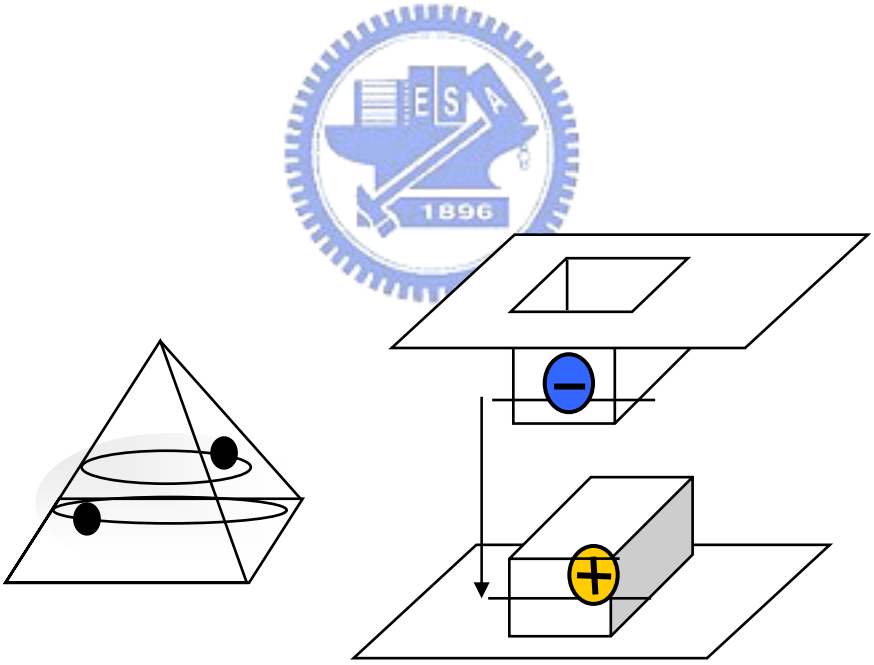

Fig 1.1.2 The carrier behavior in three dimensional confinement structure

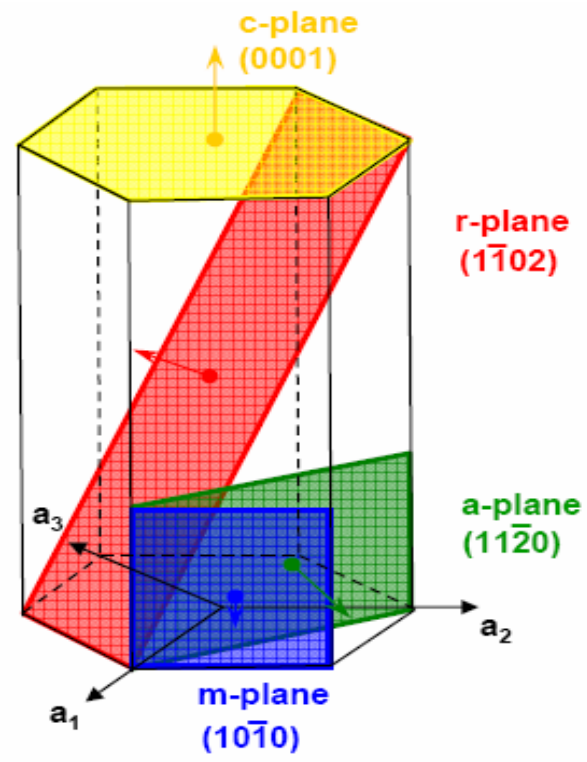

Fig 1.2.1 Different plane and orientation of hexagonal GaN

Chapter 2 Theory of GaN-based nanostructure

2.1 The formation of quantum dots structure

There are three main methods to from the quantum dot (QD) structure including Stranski-Krastanow (S-K) growth, antisurfactant method, and selective method. We summarize the growth methods in the recent years and introduce below:

(i) Stranski-Krastanow (S-K) growth mode (layer-then island)

The evolution of an initially two-dimensional growth in to a three-dimensional growth front is a well-known phenomenon and has been frequently observed in various systems. This growth mode used by various materials grown under compressive stress on heterostructure by strain-driven QD formation during heteroepitaxy as a bottom-up approach. After deposition of a few two-dimension monolayers (MLs), island structures are self-formed on a 2D wetting layer as a result of the transition of the growth mode and the stress needs to be released, as shown in Figure.2.1.1. The strain relaxation mechanisms would be first published by Stranski and Krastanow so that we called the growth mode as S-K growth mode. Especially, S-K growth has been successfully demonstrated to form self-assembled quantum dot (SAQD) on large area substrate with a good throughput and compatibility to current microelectronic technology.

(ii) Antisurfactant method

Using this growth method, the surfactant is believed to play an important role in changing the surface free energy of the sample. We can use the unequal equation to show the surface free energy for three-dimensional growth mode in a system,

$\delta s < \delta f + \delta i$,

where δs is the surface free energies of substrate, δf shows the surface free energies of film, and δi the surface free energies of film. As a third element like the surfactant is added, the sign of the unequal equal equation would be change by altering the

substrate surface free energy [16]. Using this growth method, the surfactant is believed to play an important role in changing the surface free energy of the material.

Some reports have shown the similar reversed effect occurs in GaN-based system [17-18]. The antisurfactant is believed to inhibit the film growth and intentionally modify the two-dimensional mode into-three dimensional mode. However, the role of the antisurfactant is still unknown in the element of island growth, therefore, carrying out the basic mechanism in growth way would be important for us in further detailed studies. In this thesis, antisurfactant method was used to grow InGaN/GaN QDs for the studies. The time of SiN treatment was used to control the size of quantum dot. The detail will be discussed in later chapter.

(iii) Selective method

Self-assembling growth is a convenient method to get QDs but the position of QDs is difficult to be controlled. Using selective method to obtain QDs, in the contrast, the shape, size, and the position of the QDs could be artificially designed and controlled.

In general, the selective method can control the position of the QDs by the methods of focused ion-beam (FIB) irradiation and photo-assisted wet chemical etching. S. Sakai, et al [19] grew the QDs on Si-patterned GaN/sapphire substrates. We could use different patterns to grow QDs in different shapes. Here, we simply introduce the InGaN QDs formation by selective method published by Y. Arakawa, *et al* [20]. In this thesis, after depositing three periods of InGaN MQWs on the grid-like SiO_2-GaN-saphirre patterned substrates, they believe that InGaN QDs structures are formed at the tops of the hexagonal pyramids.

Fig.2.1.2 shows a SEM top view and cross-section view of InGaN QDs structures. Shown as Fig 2.1.2 (b), no material as deposited on the SiO_2 mask and the position of the QDs were controlled very well.

2.2 Quantum confinement effect in semiconductor nanostructure

Quantum mechanism provide us an understanding of atoms, molecular, atomic nuclei and aggregation of them have both wave and partial properties within them. So-called quantum confinement effect is considering a particle confined in a finite potential whose size can be compared with its' wavelength. Let us consider the exciton in the well. If the well width is much small than the Bohr radius in bulk, no obvious confine energy is expected, because the exciton feel the same environment as in bulk. (The binding energy, Bohr radius and relative factors of bulk III-V semiconductor are listed in table 2.2.1.) If we decrease the well width at the same order or less than the exciton Bohr radius, the wavefuction and electron and hole confine in the potential well. The spatial wavefuction will be compressed in the well and it leads to enhancement of the exciton binding energy. This behavior has been demonstrated both in experiment and in theory for III-V semiconductors [21]. A brief equation given for the Hamiltonian describing the relative motion of exciton is

$$H = H_e(x,y,z) + H_h(x,y,z) + H_{e-h}(\vec{r}) \qquad \text{Eq. (2.1.1)}$$

where H_e and H_h are the Hamiltonian describing the electron and hole motion confined in the well. And $H_{e-h}(\vec{r})$ is Hamiltonian describing the Coulomb potential between electron and hole. The x-y-z coordinate is defined by the spatial confinement, and $\vec{r}$ denoted the relative position vector between electro and hole.
Then the eigenvalue can be represent given by

$$E_n = E_n^e + E_n^h - E_{e-h} \qquad \text{Eq. (2.1.2)}$$

where E_n^e and E_n^h is the energy of n_{th} quantum confined state, and E_{e-h} is the binding energy of exction.

The quantum confinement increase with reduction of the well width. In QW structure, one dimensional confinement is considered and the motion of exciton is free in the other two dimensions. For QD structure, with reducing the degree of freedom,

exciton is confined in three dimensional potential well. Thus the density of state is present in delta function. The electronic states are quantized and the energy levels become discrete. Because of the localization of carriers trapped at QDs structure where the energy separated between ground state and the first higher exciton state is larger than the thermal energy K_bT, the lifetime of the 0-D exciton strongly is almost independent of temperature.

2.3 Simulation of quantum confined Stark effect by using the FEMLAB

FEMLAB is attractive software for modeling and simulating scientific and engineering problems based on using finite element analysis to solve partial differential equations (PDE). In this thsis, the simulation was taken into account three dimensional quantum confinements for QD structure. The energy states in QDs were simply solved by self-consistent Schödinger equation. We use cylindrical symmetric coordinate to describe the QD structure for simplifying 3D problem into 2D. The general form of the Schödinger equation is described as fallow,

$$-\frac{h^2}{8\pi^2}\nabla\cdot(\frac{1}{m_e(r)}\nabla\Psi(r))+V(r)\Psi(r)=E(r)\Psi(r) \qquad \text{Eq. (2.3.1)}$$

where $m_e(r)$ is the effective mass of the well and barrier depending on different region we considered, $\Psi(r)$ is the eigenfuction of electron or hole.

For the symmetry, the function can be described by cylindrical from

$$-\frac{h^2}{8\pi^2}[\frac{\partial}{\partial z}(\frac{1}{me}\frac{\partial\chi_l}{\partial z})-\frac{1}{r}\frac{\partial}{\partial r}(\frac{1}{me}\frac{\partial\chi_l}{\partial r})]\Theta-\frac{h^2}{8\pi^2 me}\frac{x}{r}\frac{\partial^2\Theta}{\partial\varphi^2}+V_e\chi\Theta=EX\Theta \qquad \text{Eq. (2.3.2)}$$

and the wavefunction can be separated by

$$\Psi(r,z,\varphi)=\chi(z,r)\Theta(\varphi) \qquad \text{Eq. (2.3.3)}$$

We can get a general solution is

$$\Theta=\exp[il\varphi] \qquad \text{Eq. (2.3.4)}$$

where l denote the quantum number of different energy levels. And we substitute the solution in the original equation and simplify it as fallow,

$$-\frac{h^2}{8\pi^2}\frac{\partial}{\partial z}\left(\frac{1}{me}\frac{\partial \chi_l}{\partial z}\right)-\frac{h^2}{8\pi^2}\frac{1}{r}\frac{\partial}{\partial r}\left(\frac{1}{me}\frac{\partial \chi_l}{\partial r}\right)+\frac{h^2}{8\pi^2 me}\frac{l^2}{r^2}\chi_l+V_e\chi_l=E_l X_l \qquad \text{Eq. (2.3.5)}$$

Finally, we can use this equation and substitute the corresponding factor in the general form of software to obtain the eigenfuction and eigenvalue. The detail calculation of InGaAs QD is described by R. Melnik *et a*l [22]. In our simulation, the bowing factor of calculating the band gap used as 1.4 eV and the band offset ratio was assumed to be 60 : 40 [23-24]. As a result the potential of conduction and valence band is defined as

$$\begin{aligned}\Delta E_c &= Eg\times 0.6\\ \Delta E_v &= Eg\times 0.4\end{aligned} \qquad \text{Eq. (2.3.6)}$$

And the effective mass of InGaN is used by the linear combination of InN and GaN.

$$\begin{aligned}m_e^{InGaN} &= x m_e^{InN}+(1-x)m_e^{InGaN}\\ m_h^{InGaN} &= x m_h^{InN}+(1-x)m_h^{InGaN}\end{aligned} \qquad \text{Eq. (2.3.7)}$$

where x is the In composition of InGaN.

The simulation results of InGaN/GaN QD structure are shown in Figure 2.3.2 (a), (b) and (c). Those figures demonstrate electron wavefuction in ground states, first excited and second excited states. The existing probability of carrier is found to confine in the QD with lower potential than barrier region. One the other hand, the corresponding eigenvalue of electron or hole can be obtained in the software.

As the QD size was increasing, the energy levels of quantized sub-band become smaller. The relation was shown in Figure 2.3.3 when we consider the InGaN QD with 3 nm and 10 nm in diameter and height. The quantum confinement energy was almost proportional to L^{-2}, where L was the potential dimension. And the build-in fields under electric field 0, 0.25, 0.5 M Vol/cm^2 are considered. The build-in field is found to result in the reduction of resonance energy. The wavefution of electon attend to exist in one side of bending potential. Under larger built-in field, the obvious

dependence on the well width can be recognized in the figure 2.3.3.

2.4 The localization effect in quantum well structure

In InGaN-based structure, the high luminescence efficiency is due to In-rich regions within InGaN layer. These In-rich regions are believed to act as In-rich QDs in the InGaN layer, providing deep potential wells that suppress the diffusion of electrical carriers toward various nonradiative defects and result in a large red shift in the emission energy.

The behavior of In-rich or QDs like region in InGaN QWs are a unique characteristic and the origins of Indium segregation are not very clear until now. There are several suggestions to explain the production of In rich cluster and relative QD-like structure. One of the possibilities is resulted from the compositional fluctuation. The compositional fluctuation of indium is commonly observed in the majority of InGaN alloys. Another possibility is resulted from phase separation. Theoretical calculations predict that phase separation in an InGaN layer occurs below the critical temperature and for a range of composition of the alloy that defines a miscibility gap at a given growth temperature. Otherwise, in the experimental results, In-rich QDs formed by phase separation have been observed in InGaN films that contain high concentrations of In or a layer thickness larger than the critical layer thickness. Moreover, InGaN MQW always has a so-called V-defect consist of treading dislocation. It has been proposed that the V-defect was proposed to attach with and associated with In-rich regions. Cremades *et* al [24] suggested that the built in strain in InGaN layers determines the preferential incorporation of In atoms to the ally in the regions where the strain is relax thus resulted in the formation of defect.

2.5 The basic concept of nonpolar stucture

Wurzite GaN-based structure grown in nonpolar orientation is attracting attention owing to less influence of the built in field in QW. The built in field is the sum of spontaneous polarization and strain induced piezoelectric field. In this section, the basic concept of nonpolar structure will be discussed. The structure diagram of hexagonal structure has been demonstrated in Fig 1.1.3. In normal, nonpolar structure can be developed on two growth method. The first approach is growing [1100] oriented m-plane GaN template on closely lattice matched [100] plane of $LiAlO_2$ by hydride vapor phase epitaxy and molecular beam epitaxy [7]. The Second is growing $[11\bar{2}0]$ oriented a-plane GaN template on r-plane sapphire or $[11\bar{2}0]$ SiC by metalorganic vapor-phase (MOVPE) [8]. These two methods has been successfully developed on AlGaN/GaN and InGaN/GaN MQW structure [26-27]. Based on conventional structure, the build in field is supplied by strain induced piezoelectric field and spontaneous polarization field. The build in field of GaN based structure is induced from Ga and N atoms which arranged parallel growth axis in normal c-plane films. The piezoelectric and spontaneous electric fields are at the opposite direction as shown in Figure 2.5.1. However, nonpolar structure was applied to enhance the internal quantum efficiency due to not affected by polarization effect based on the direction of Ga and N atoms arrange normal to the growth axis. As a result, the build in electric field is normal to the direction of QW. The potential can not be influenced by the polarization and its shape keep on flat as shown in Fig 2.5.2 The wavefuciton overlap of electron and hole is larger than c-plane GaN.

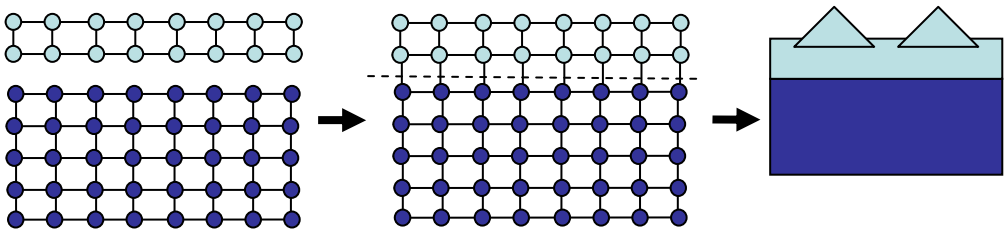

Fig 2.1.1 The diagram of strain relaxation for S-K growth mode

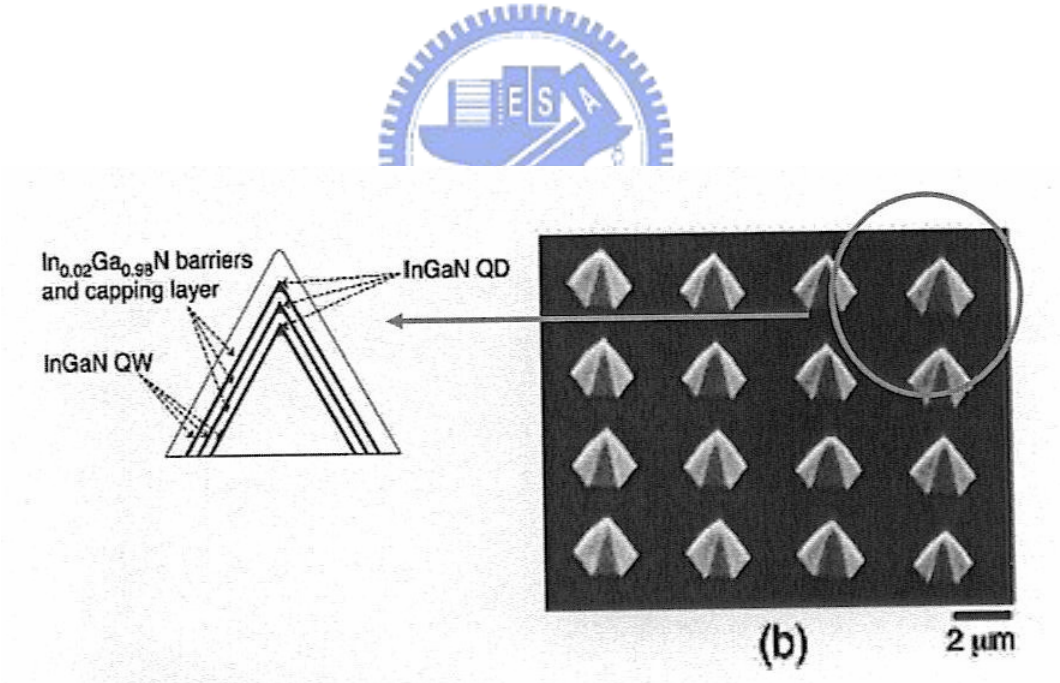

Fig 2.1.2 A SEM top-view and cross-sectional view (b) of InGaN QD structures

	GaN (Wurtzite)	GaAs	In_xGaN_{1-x}
m_e	0.2	0.063	0.11x+(1-x)0.2
m_{hh}	0.8	0.51	1.61x +(1-x)0.8
$\frac{1}{\mu}=\frac{1}{m_e}+\frac{1}{m_{hh}}$	0.16	0.056	$1/\mu$ μ is described as the below diagram
ε_r	8.9	12.9	8.9
Eb (mev)	27.5	4.58	27.5× (μ/0.16)
Bohr radius (nm)	2.94	12.17	2.94×(0.16/μ)

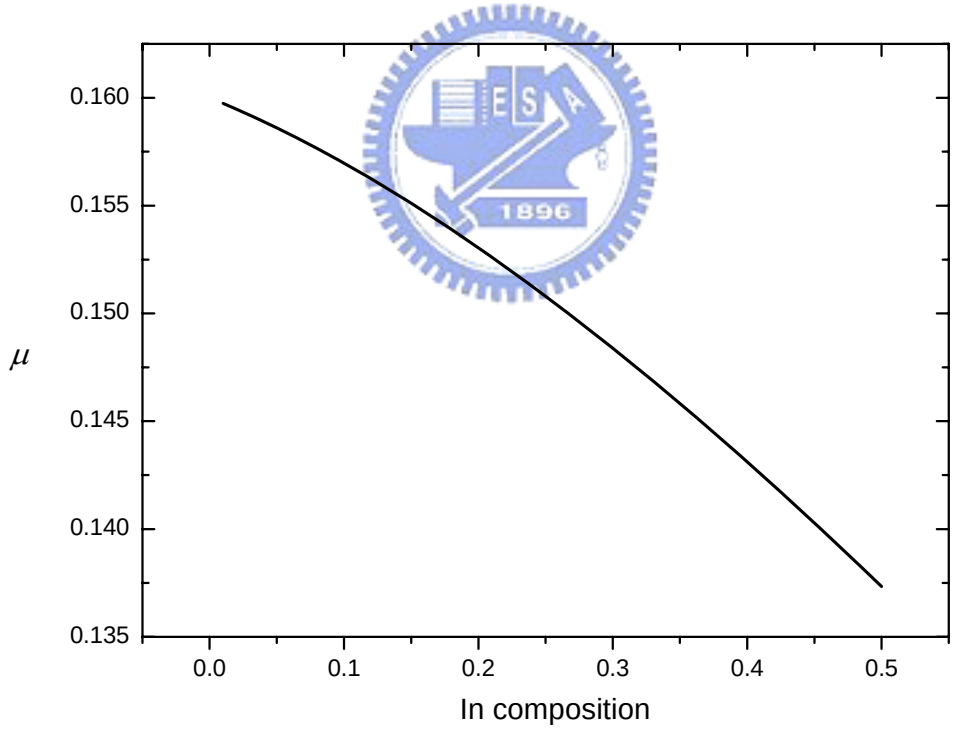

Table 2.2.1 Binding energy and relative simulation factors of III-V semiconductors

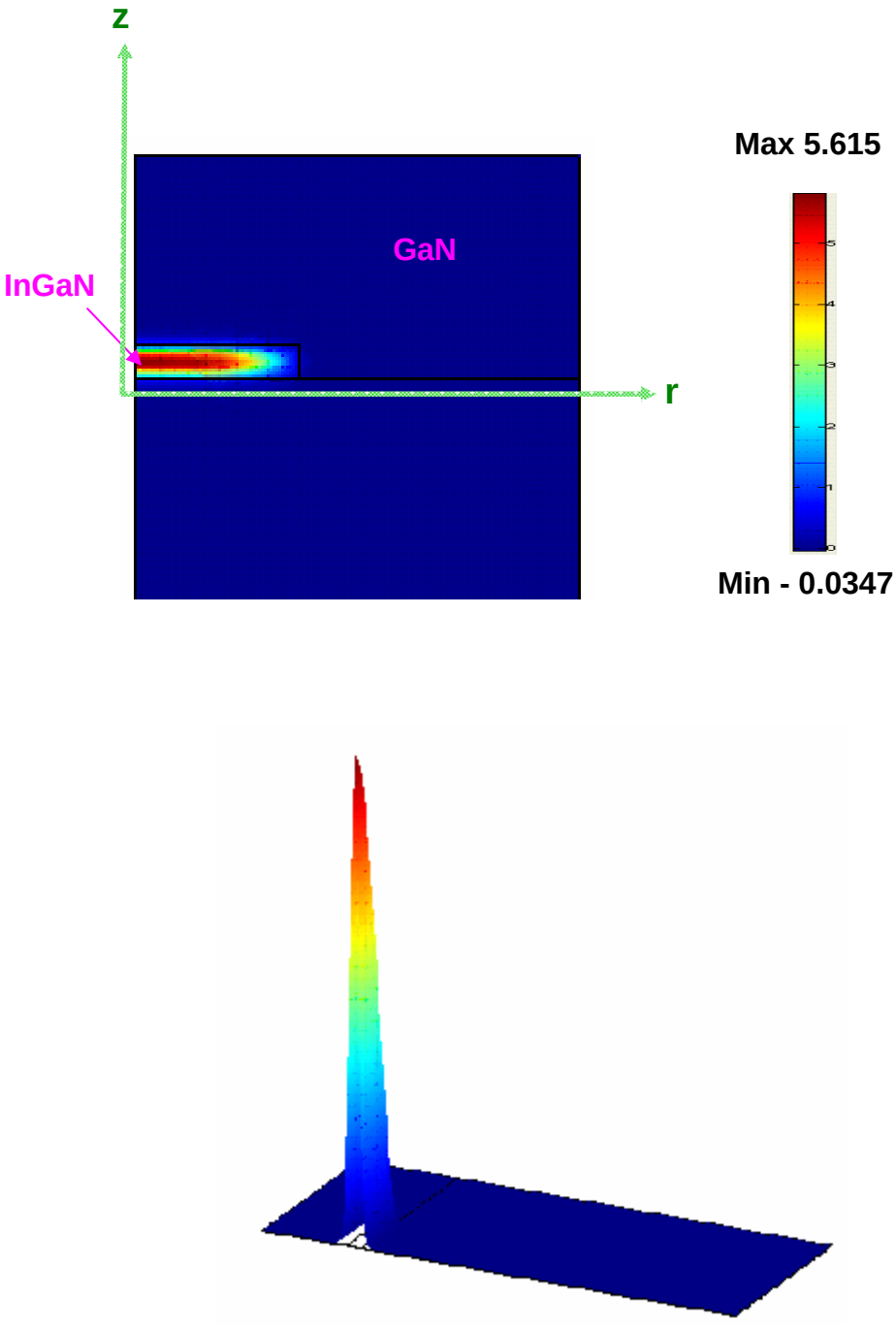

Fig.2.3.1 (a) Wavefunction of electron in ground state

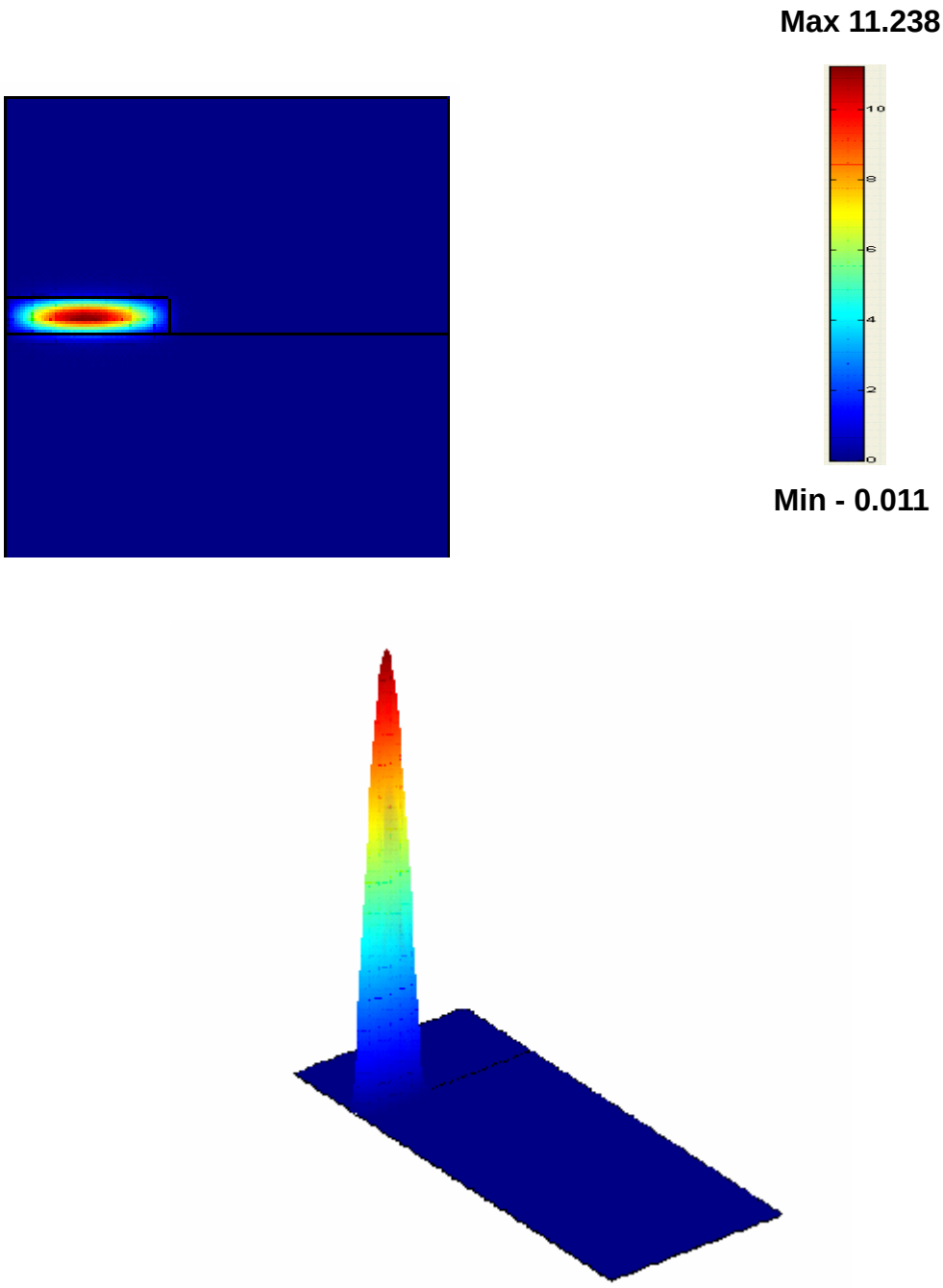

Fig.2.3.1 (b) Wavefunction of electron in first excited state

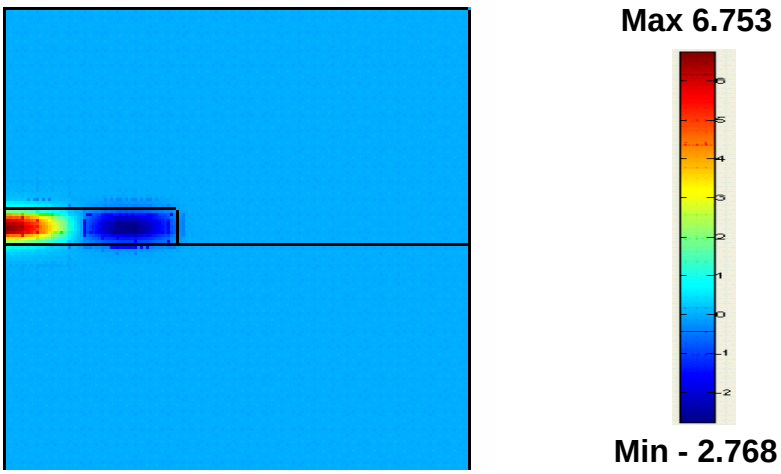

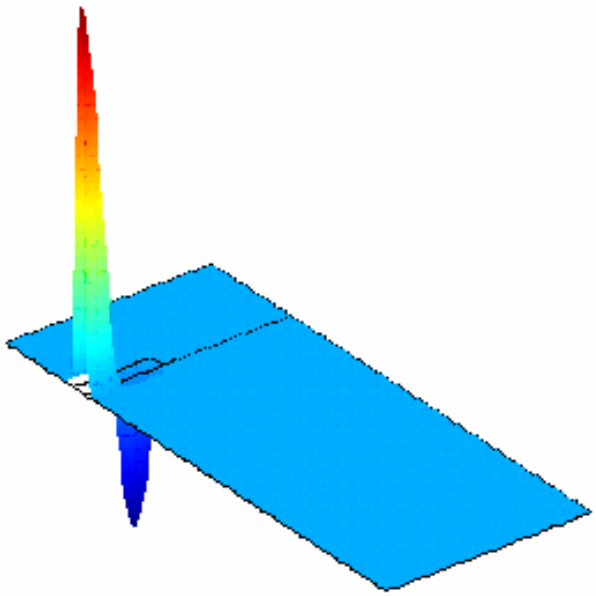

Fig.2.3.1(c) Wavefunction of electron in second excited state

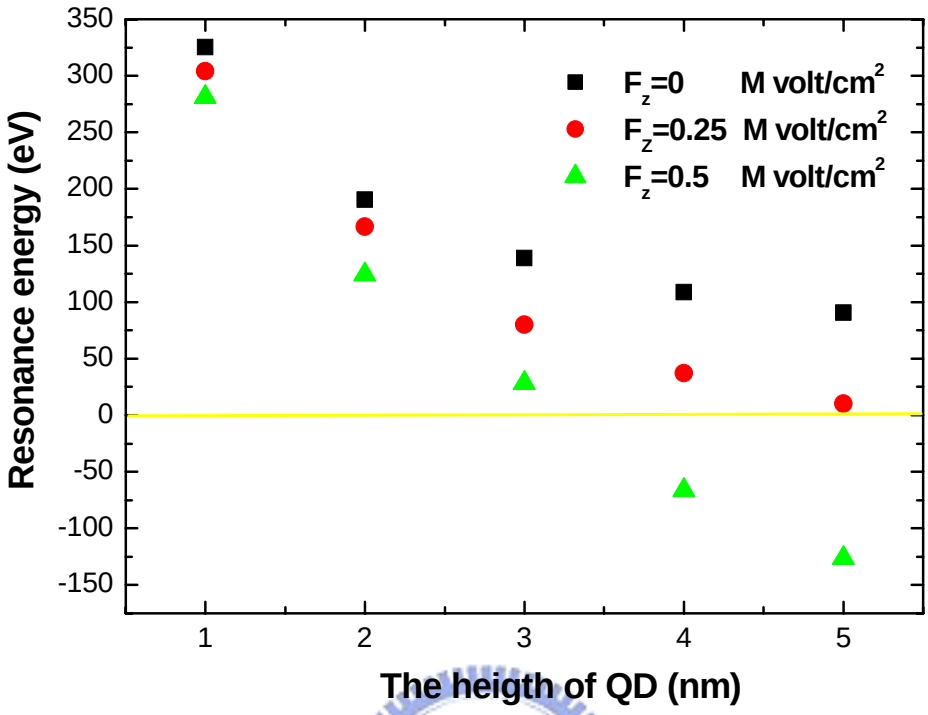

Fig.2.3.2 Well width dependence of the ground state resonance energies in the single QD model under electric field 0, 0.25, 0.5 M Vol/cm^2

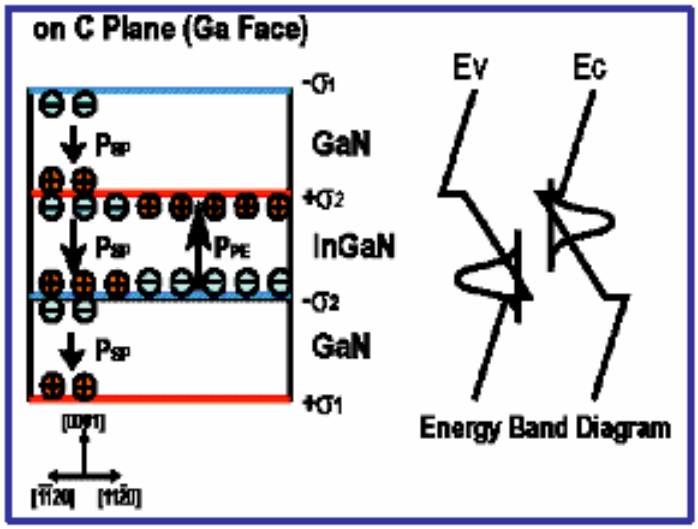

Fig.2.5.1 Band diagram of c-plane InGaN/GaN MQW

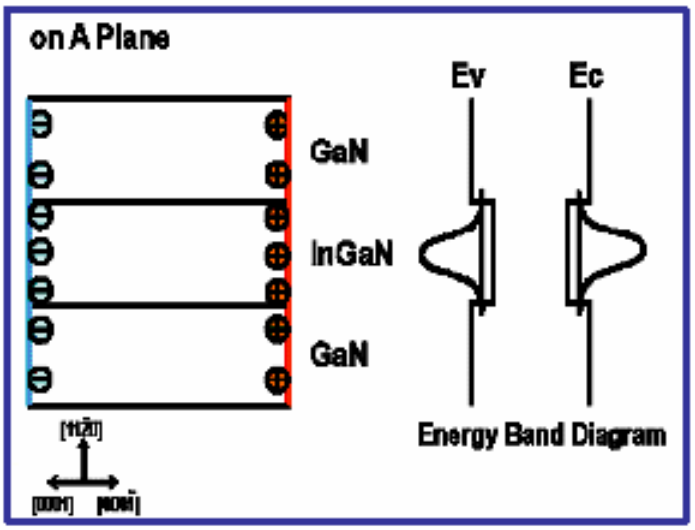

Fig.2.5.2 Band diagram of a-plane InGaN/GaN MQW

Chapter 3 Experimental principle and Experiment Setup

3.1 Photoluminescence (PL)

Photoluminescence is the emission of light from a material under optical excitation. The energy of the laser light should be shorter than the band gap energy of the semiconductor. The exciting source is absorbed by semiconductor and the electros in conduction band and holes in valance band generated under excitation. When an excited electron in an excited state returns to initial state forming a photon a photon whose energy is the difference between the excited state and the initial state energies, then we detect the PL signal. In order to reach equilibrium, the carriers will recombination in many ways. The processes can be direct or indirect depending on the band gap energy of the material. The PL spectra are obtained by analyzing the spectral elements of the emitted light. Depending on the type of the band gap the transition can be classified into direct transition and indirect transition. The combination of indirect transition related to the phonon scattering which results in the momentum and the energy transition.

Typical radiative recombination processes in semiconductors occur in many ways, PL emission of those transitions can be recognized easily at low temperature exclusive of the thermal energy. The exciton was generated by of electron and hole pair which bounded by the coulomb interaction. Luminescence of high purity and high quality semiconductors is dominated by free exciton (FE) emission, normally refereed to a Wannier-Mott exciton [28]. The FE emissions from h-GaN at low temperature have been observed in the early 1970s. There are many forms of exciton bounded to other particles. An exciton bound to a neutral donor and is in general called a bound excton (BE). Similarly, neutral acceptors always produce exciton bound to them. The transition energy of BE is lower the binding energy than that of FEs [29]. The simultaneously existence of doner and acceptor impurities introduce a

pair called doner-acceptor pair (DAP) recombination.

The setup of our PL system is shown in Figure 3.3.1. The pumping light source was multi-mode and non-polarized Helium-Cadmium laser operated on 325nm with 20mW. After reflected by three mirrors, the laser light was focus by a lens which focal length was 5cm, to 0.1 mm in diameter and the luminescence signal was collected by some lens. The probed light was dispersed by 0.32 monochromator (Jobin-Yvon Triax-320) equipped with 1800, 1200, and 300 grooves/mm grating and which maximum width of the entrance slits was 1mm. The resolution was controlled in 1nm by selecting 300 grooves/mm grating and slit of 0.1 mm. We use long pass filter in order to avoid the laser coupling with the PL spectrum.

3.2 Photoluminescence Excitation (PLE)

In PL measurement, which is performed at fixed excitation, is performed at fixed excitation energy, the luminescence properties are generally investigated. While PL excitation (PLE) spectroscopy, which is carried at fixed detection energy, provides mainly information about the absorption properties. Apart from absorption and PL experiment is widely used spectroscopic tool for the characterization of optical transitions in semiconductors. It is very important to note that the PLE also depends strongly on the different carrier relaxation processes. Nevertheless, in many cases it is difficult to separate the influence of relaxation from that of absorption. The PLE spectrum is strongly influenced by the relaxation depending on different samples.

The setup of PLE is shown in Figure 3.3.2.The pumping source of PLE was Xe lamp with 450W separated by double-grating monochoramator (Jobin-Yvon Gemini 180) and then coupled to samples at an angle about 45˚ by two focal lenses. We fixed the detection energy of the spectrometer Triax 320, and changed the excitation energy of Xe lamp from 300 nm to the band gap of each sample. At the exit of the

spectrometer Triax 320, a high sensitive Hamamatsu photomultiplier tube (PMT) with GaAs photocathode was placed to detect the luminescence signals.

3.3 Atomic Force Microscopy

Atomic force microscopy (AFM) images the surface of a sample by scanning a sharp tip (10um in long and small than 10nm in diameter) over and measuring the deflection of the tip. The fundametal setup of AFM is illustrated in Fig 3.3.3. A piezoelectric controller moves the sample in x-y direction under the tip. The position of the tip is measured by reflecting laser from the backside of the cantilever to a split photodiode. Depending on the distance between the tip and the sample so that the force acting on the tip is replusive, the AFM work in contact mode. In non-contact or taping mode the tip is futher away from the sample and in the rigium of an attrative froce [30]. The cantilever is set to vibration close to its resonant frequency and change in the surface morphology lead to changes in the frequency, which can be measured sensitively.

3.4 Rapid Thermal Annealer

The rapid thermal anneal (RTA) system were used to investigate the post-grown thermal annealing effect, it was heatpulse 610i rapid thermal processing system. The RTA temperature range is from 400˚C ~ 1250˚C and the duration of maximum time up to 300 seconds.

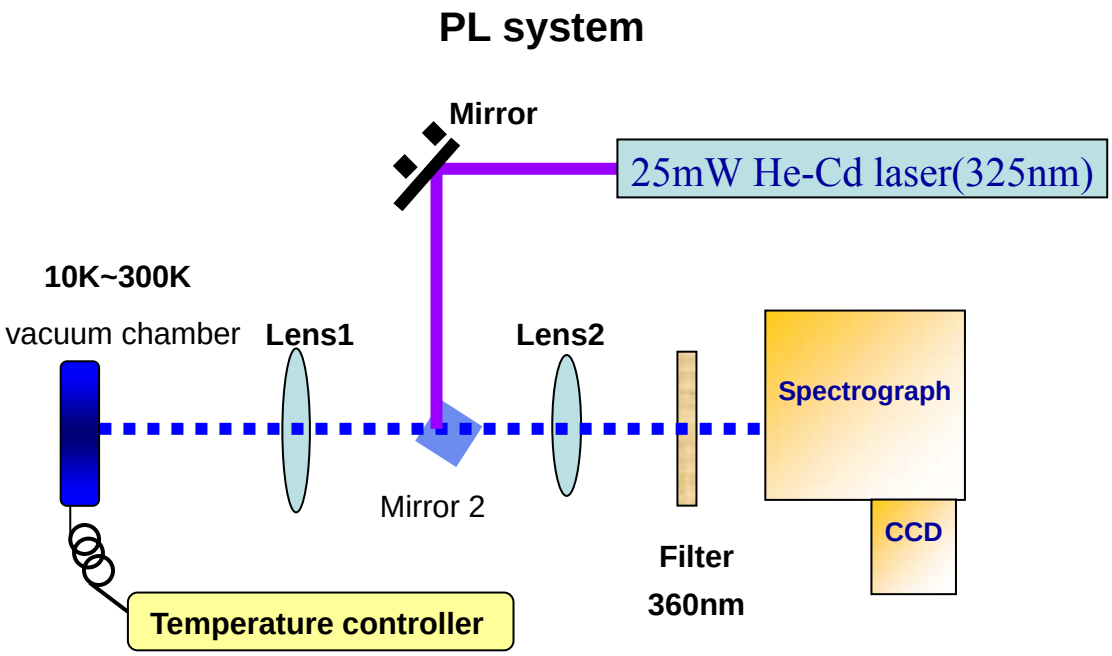

Fig. 3.3.1 The setup of PL system

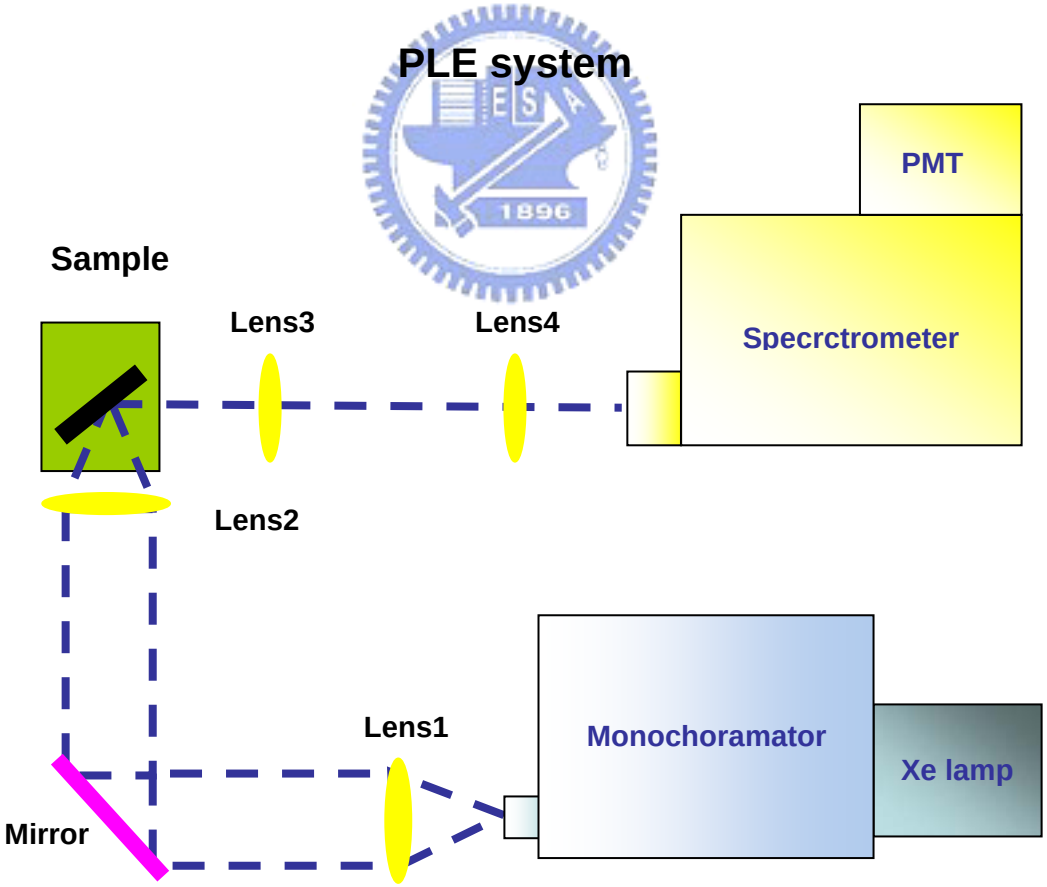

Fig. 3.3.2 The setup of PLE system

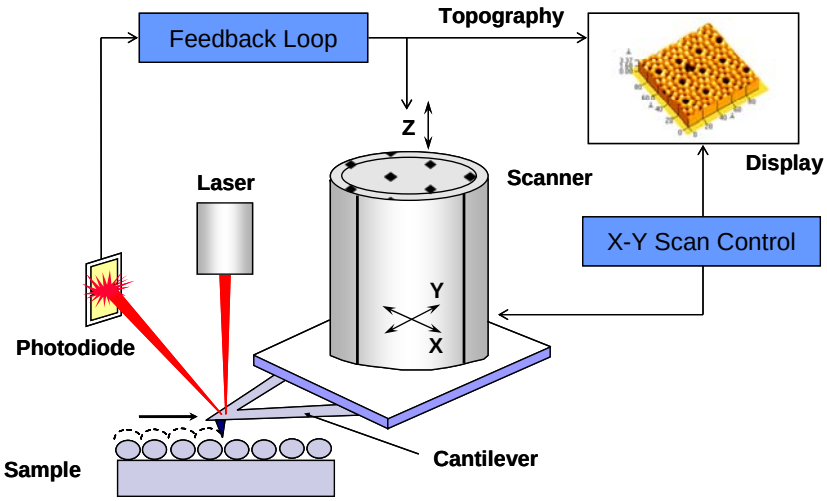

Fig. 3.3.3 The fundametal setup of AFM

Chapter 4 Optical Properties of InGaN Quantum Dots

4.1 Introduction

Recently, InGaN alloy is a potential material for realization of blue-green light emitting diodes and laser diodes [1-3]. Quantum dot (QD) structure as active layers could be applied in these optical devices to reduce the threshold current and enhance emitting efficiency due to three-dimensional confinement of carriers and delta-like density of state [4-5].

Moreover, in the fabrication process of optical devices, thermal annealing is an important technique to improve their performance. For example, the growth temperature of InGaN multiple quantum wells (MQWs) and p-type Mg doped GaN layer is 780 ˚C and 1050 ˚C, respectively. After deposition of a p-typed Mg doped layer, samples should be thermally annealed in N_2 ambient at 750 ˚C or higher to remove hydrogen incorporation for activation of the Mg dopant to obtain higher conductivity [31]. In order to achieve the ohmic contact between GaN and metal, thermal annealing at 450 ˚C to 950 ˚C is applied to lower the contact resistance [32]. However, the optical properties would be changed in the high temperature process. Therefore, studies on post-growth thermal annealing will provide useful information for us to design process procedures and adjust the desired emission wavelength. The effects of thermal annealing on optical properties of InGaAs/GaAs and InAs/GaAs quantum dots (QDs) have been widely investigated [33]. In InGaN QW, the effects of thermal annealing on dot-like structures have also been studied [34]. However there are few reports on optical properties of thermally annealed InGaN QDs grown by three dimensional growth methods.

In this report, the characteristic of InGaN/GaN QDs with two different sizes have been studied in their structure and emission properties by photoluminescence (PL) and atomic force microscopy (AFM) measurement and theoretical simulation. Small

QDs with apparent quantum confine effect exhibited blue shift on PL peak than the larger QD. Theoretical simulation agreed with this result. The effects of thermal annealing on optical properties of InGaN/GaN QDs were investigated by rapid thermal annealing (RTA) system and PL measurement, When annealing temperature increased from 650 ˚C to 950 ˚C, a red-shift followed by a blue-shift on PL peaks emitted from InGaN/GaN QDs was observed. Theoretical simulation and temperature dependent PL measurement were used to analyze the mechanism of the InGaN/GaN QDs of thermal annealing.

4.2 Sample preparation

The investigated samples were grown on (0001) c-face sapphire substrates by metal-organic chemical vapor deposition (MOCVD). A 30-nm-thick low-temperature GaN nucleation layer was grown at 550 ˚C followed by a 2-μm-thick Si-doped n-GaN underlying layer grown at 1000 ˚C. Before the InGaN was grown, NH_3 and diluted Si_2H_6 were mixed to form SiN_x on the GaN surface with the treatment time of 160 and 195 seconds for sample A and sample B, respectively. During the treatment time, the SiN_x film would form nano-masks for the subsequent InGaN QDs growth. Therefore, the formation of InGaN QDs could be controlled by adjusting the treatment time of SiN_x. Finally, each sample was capped with a 10-nm-thick un-doped GaN layer. The sample structures for un-capped and capped were shown in Fig 4.2.1(a) and Fig 4.2.1(b). To study the surface morphology on InGaN QDs, atomic force microscopy (AFM) images of uncapped as-grown InGaN QDs were shown in Fig. 4.2.2 (a) and (b) for sample A and sample B, respectively. The ultra-high density of InGaN QDs was estimated to be about 3×10^{11} cm^{-2} for both samples. The height/diameter of sample A and sample B were 1.8 nm / 35.2 nm and 2.9 nm / 30.5 nm. The QD size was enlarged with increasing the SiN_x treatment time.

4.3 Surface morphology of InGaN QDs

The surface morphology of sample A and B were characterized by AFM. Scans were performed over a surface area of 500 nm, using a digital instrument microscopy with a sharp tip. In Fig 4.2.1 (a) and Fig 4.2.1 (b), AFM images of uncapped sample A and B are shown. AFM images were performed over a surface area of $1\mu m \times 1\mu m$. The average lateral size and height of sample A are about 35.2 nm and 1.8 nm. As increasing the SiN_x treatment time, the QD sizes become larger, 1.8nm in height and 35.2nm in diameter for sampleB. The densities of different size QDs ere estimated to increase approximated from $2.1 \times 10^{11} cm^{-2}$ and $2.9 \times 10^{11} cm^{-2}$. The ultra high density is much larger than the dislocation density. This means that the main parts of the QDs are free of defects. This is useful for achieving high efficiency emission.

4.4 Photoluminescence of InGaN quantum dot with different sizes

PL measurement were excited by a He-Cd laser and detected by a charge-couple detector (CCD). The wavelength and power of exciting source are 325 nm and 25 mW. Fig 4.4.1 shows the corresponding normalized PL spectra at room temperature (RT) for sample A and sample B. The dominant PL peak for two as-grown QDs are 434.4 nm (2.855 eV) and 472.3 nm (2.625 eV), respectively, witch show a clear red shift with the duration of SiN_x treatment. The SiN_x treatment time and PL peak energies with each sample are listed in Table 4.4.1. The red shift can be attributed by the increasing the QD sizes due to quantum confined effects of low dimension structure. In order to confirm our experimental results, energy states of QDs were solved by self-consistent Schrödinger equation. From our simulation calculation, three-dimensional confinement was taken into account for calculating the eigenvalues. The transition energies were estimated to be 2.847 eV and 2.633 eV for sample A and sample B, respectively. In Fig 4.4.1 the transition energy from ground state of

conduction band to valance band witch is denoted by ec1-hh1 was demonstrated. The deviation between the calculated and measured value was less than 3%. Therefore, the peak position of sample B with a red shift compared with sample A could result from larger vertical size, thus decreasing quantum confine energy.

4.5 Optical properties of thermal annealing on InGaN QDs

4.5.1 Sample preparation

The post-growth thermal annealing effect on the optical properties was investigated by PL measurement. He-Cd laser was used as an excitation source and the PL signal was detected by a charge-couple detector (CCD). The wavelength and power of the excitation source were 325 nm and 25 mW. To study the effects of thermal annealing on the InGaN QDs, we prepare sample A and sample B with the treatment time of 160 and 195 seconds, respectively. As-grown samples were thermal annealed using the RTA system at 650 ˚C, 750 ˚C, 850 ˚C, and 950 ˚C in one minute.

4.5.2 Study of photoluminescence at different thermal annealing condition

The PL spectra for as-grown samples were shown in Fig. 4.2.3. The PL peaks of sample A and sample B are 434.4 nm (2.855 eV) and 472.3 nm (2.625 eV) measured at room temperature, respectively. The PL peak of sample B with a longer SiN_x treatment time exhibits a lower emission energy in comparison with sample A. PL peak positions were extracted by Gaussian fitting to eliminate Fabry-Perot effect. Figure 4.5.1 shows measured PL peaks of InGaN/GaN QDs for two samples annealed at temperature from 650 ˚C to 950 ˚C in one minute. For sample A, thermal annealing leaded to an obviously red-shift of about 18.6 meV until 750 ^{o}C. However, higher thermal annealing temperature ranged from 750 ^{o}C to 950 ^{o}C caused a blue-shift of 29.4 meV. For sample B, a smaller red-shift of about 5.7 meV on the PL peak was

observed followed by a blue-shift of about 26.9 meV.

4.5.3 The simulation of diffusion effect on InGaN QDs

The simulation was introduced to study the mechanism of PL peak shifting. The diffusion length, a function of annealing temperature, was defined as [35],

$$\ln(L_d{}^2 - L_{d_0}{}^2) = -\frac{Ea}{K_B T} + \ln 4t \qquad \text{Eq. (4.5.1)}$$

where T is the annealing temperature, t is the annealing time and L_{d_0} is an initial boarding factor.

According to this function, increase of the annealing temperature can be seen as increase of the diffusion length. Upon thermal annealing, indium diffuses out of the QD into barriers. The sizes of QDs increase and the potential profiles change at the same time. Both effects influence the transition energy. In Fig. 4.5.2, the simulation result implied that the transition energy exhibited a red-shift then followed by a blue-shift with increasing the diffusion length, i.e. increasing the annealing temperature. From the diffusion model, the potential profile revealed that diffusion occurred from the edge of QD at the beginning. The potential depth at the center of QD remains almost unchanged but the QD size increases in the small diffusion length, which reduced the quantum confined energy and resulted in a red-shift of the emission peaks. As increasing the diffusion length, the decrease of the indium composition and the barrier height resulted in a blue-shift of the emission peaks gradually. PL peaks of sample A which has a smaller QD height subjected to thermal annealing exhibited a larger red-shift than sample B. As the diffusion length was increased, QD size was enlarged. The quantum confinement energy was proportional to L^{-2}, where L was the potential dimension. As a result, the decrease of quantum confinement played a more important role in the small QD. Furthermore, another

possible reason contributed to the red-shift of the peak positions was the reduction of the compositional fluctuation after the thermal annealing [36]. Low miscibility between InN and GaN leads to the segregation of indium. Diffusion from the In rich region to the surrounding In deficient region could reduce the average composition in the QD and contribute to a part of the red-shift of emission peaks.

4.5.4 Temperature dependent PL

Temperature dependent PL measurements provided us information about the variation in size and potential after thermal annealing. Sample A (with a smaller QD size in comparison with sample B) was annealed at 750 ^{o}C for nine minutes. The temperature dependent PL results of the as-grown samples and annealed samples are demonstrated in Fig. 4.5.3. The energy-shift was taken to be zero at 20 K. In the observation temperature ranged from 20 to 300K, the as-grown sample exhibited a total red-shift of 14.5 meV on PL peaks which was smaller than that of the annealed sample (20.3 meV). Temperature dependent variation in the band gap energy could be explained by Fröhlich interactions which took into account the LO phonons coupling with polar excitons [37]. Smaller QD had a stronger quantum confinement which could compress the exciton Bohr radius. Compression of the Bohr radius made less polarity of excitons and reduced the coupling with LO-phonons [38-39]. Therefore, a larger red shift of the annealed QD sample in the temperature dependent experiment confirmed that QD size increased after thermal annealing. Moreover, in Fig. 4.5.4, thermal activation energy can be extracted based on the band tail model suggested by Eliseev *et al.* as followed [40],

$$\frac{I}{I_0} = \frac{1}{1 + A\exp(-\frac{E_a}{kT})} \qquad \text{Eq. (4.5.2)}$$

The activation energies, *Ea*, were estimated to be about 75.2 and 54.9 meV for

as-grown and annealed samples, respectively. Decreasing in activation energy of the annealed InGaN QDs indicated the less confinement of carriers due to the barrier height decrease caused by the out-diffusion of the In atoms from the QDs. Temperature dependent PL experiments further supported that thermal annealing would increased QD size and decreased potential depth in the QD.

4.6 Conclusion

In conclusion, we have investigated the optical characteristic of ultra-high-density InGaN QDs grown by MOCVD. AFM revealed that the extremely high density about 3×10^{11} cm^{-2} of QDs was obtained and the size of QDs was increased with the duration of SiNx treatment. The PL peak energy was decrease with increasing the QD size due to reduction of quantum confine. In addition, we have investigated effects of thermal annealing on the optical properties of InGaN/GaN QDs by PL measurement and theoretical simulation. A red-shift followed by a blue-shift of PL peaks of InGaN QDs was observed as increasing the annealing temperature. The variation of transition energy was contributed to the enlargement of QD and reduction of barrier height. The former contributed to a red-shift and the later contributed to a blue-shift of the emission peaks. Finally, temperature dependent PL experiments further supported that thermal annealing would increase QD size and decrease potential depth in the QD.

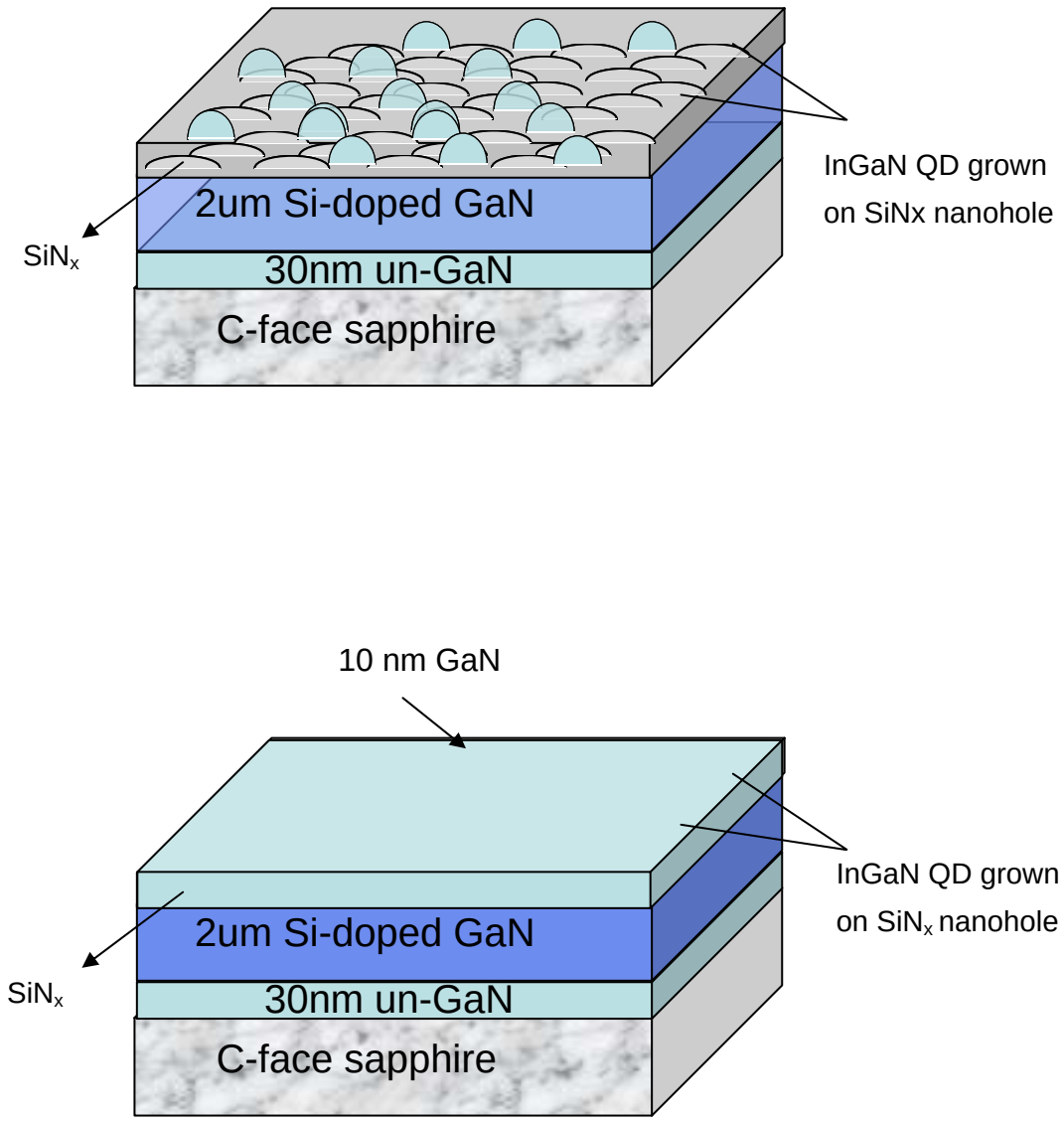

Fig. 4.2.1 The InGaN QD sample structure (a) un-capped sample for AFM measurement (b) capped sample for optical measurement

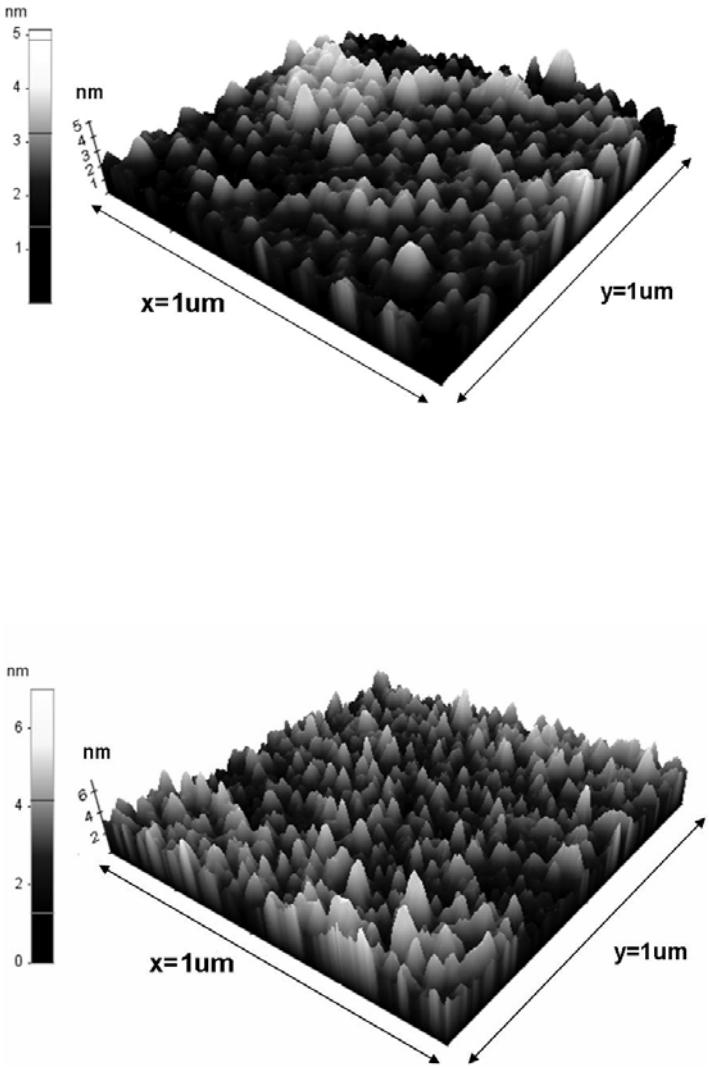

Fig. 4.2.2 Surface morphology of as-grown InGaN QDs scanned by AFM measurement. (a) Sample A: Small QDs with average height/diameter (1.8 nm/35.2 nm) (b) Sample B: Large QDs with average height/diameter (2.9 nm/30.5 nm)

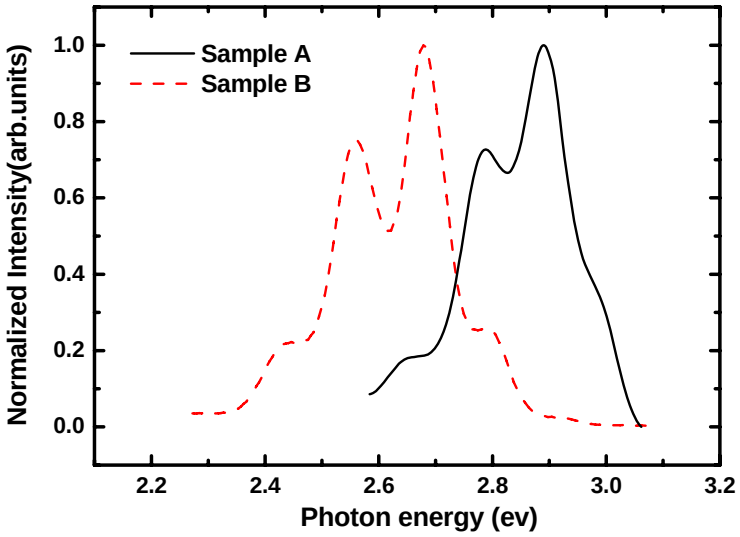

Fig. 4.2.3 Room temperature PL spectra of sample A (solid line) and sample B (dash line)

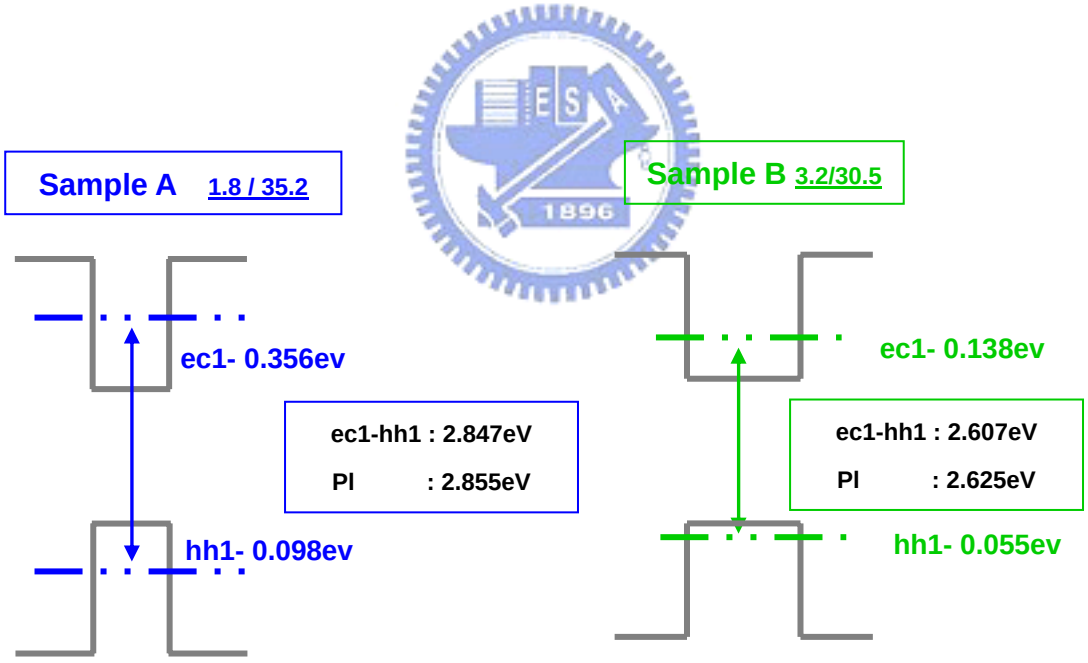

Fig. 4.4.1 The diagram of transition levels for sample A and sample B

	Sample A	Sample B
SiN_x treatment time (s)	160	195
QDs height (nm)	1.8	3.2
Experimental PL peak energy (eV)	2.854	2.633
Simulated PL peak energy (eV)	2.847	2.607

Table 4.4.1 The summary of the growth condition along with optical properties for sample A and sample B.

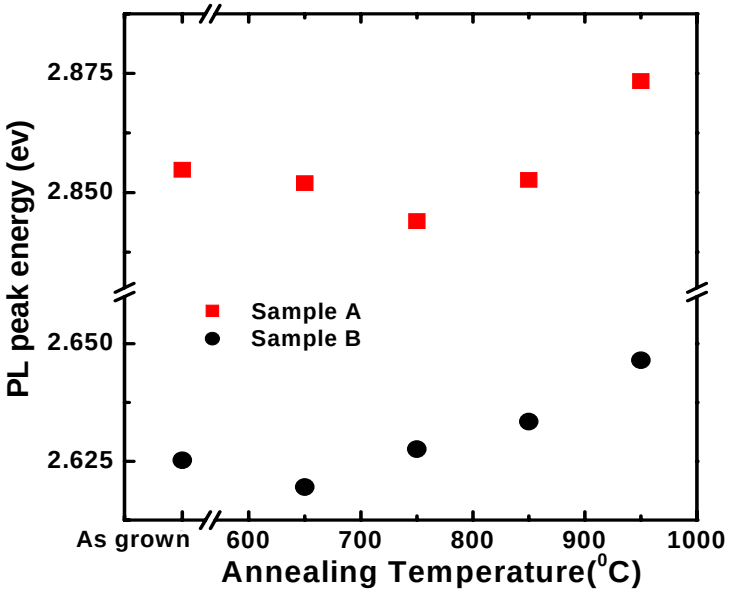

Fig. 4.5.1 Energy shift versus annealing temperature for sample A (rectangular) and sample B (circle)

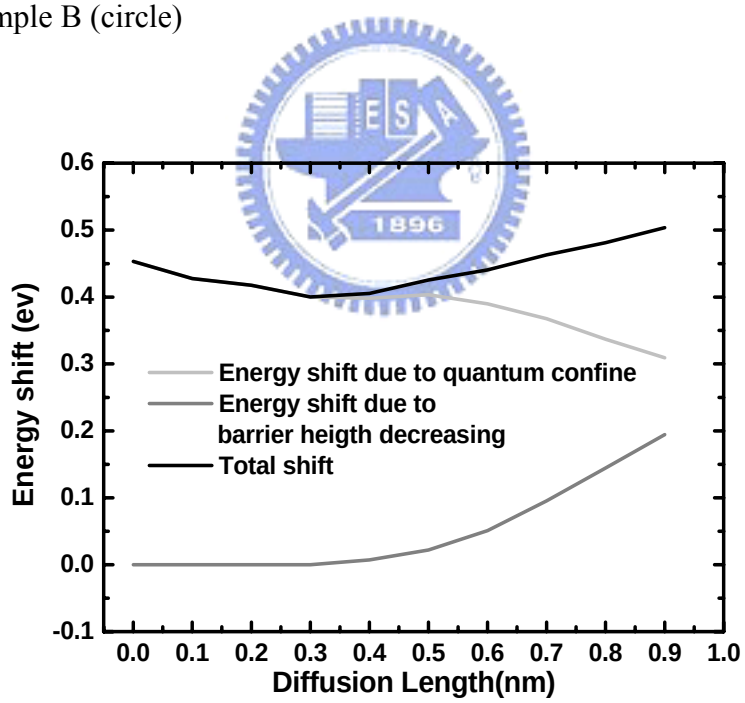

Fig. 4.5.2 Simulation results of energy shift as a function of diffusion length for 1.8/30 nm InGaN/GaN QDs. Total shift (solid) can be combined with two effects, a red shift (dot) induced by quantum confined effect and a blue shift (dash) induced by decrease of the barrier height

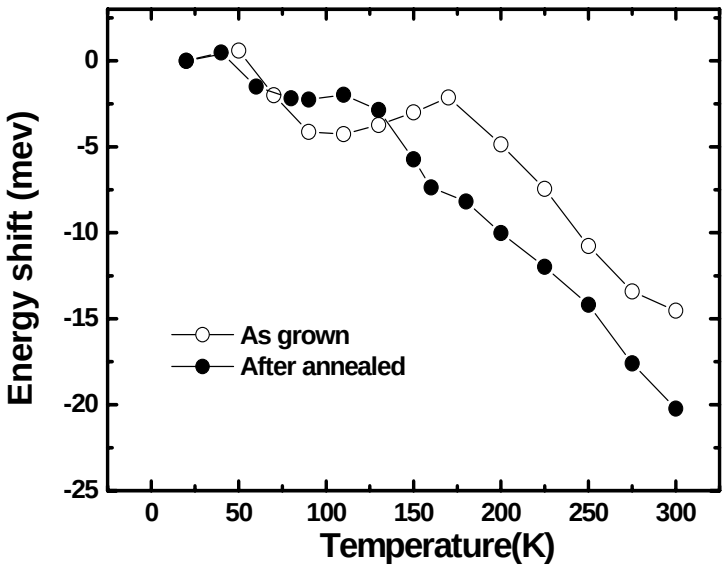

Fig. 4.5.3 Energy shift in temperature dependent PL measurement ranged from 20 K to 300 K for as-grown and annealed QDs samples

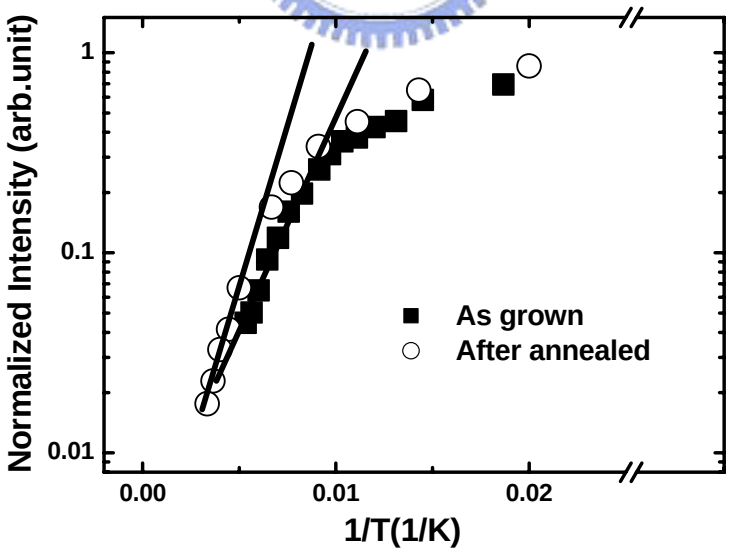

Fig. 4.5.4 Arrhenius plot of the integrated PL intensity for as-grown and annealed QDs samples

Chapter 5 Optical Properties of a-plane InGaN/GaN Multiple Quantum Wells on r-plane sapphire

5.1 Introduction

The quantum efficiency of light emitting diodes (LEDs) and laser diodes (LDs) based on group-III nitride heterostructures is reduced due to the presence of built-in electric fields on polar structure. This built-in electric field induces the quantum -confined Stark effect in the quantum well. This effect decreases the radiative recombination and reduces the oscillator strengths due to the separated wavefuction of electrons and holes [41]. Recently, Nonpolar structure was applied to enhance the internal quantum efficiency due to not affected by polarization effect based on the bonding of Ga and N atom is along [1000] axis and orthogonal to the growth axis. As a result the influence of the internal build-in electric field on the quantum well direction can be neglected. Nonpolar structure was successfully developed by growing $[1\bar{1}00]$ oriented m-plane GaN on [100] oriented r-plane $LiAlO_2$ or $[11\bar{2}0]$ oriented a-plane GaN on [100] oriented r-plane $LiAlO_2$. The structure of GaN/AlGaN MQWs with m-plane orientation have been analyzed in the effects of built-in electrostatic field in determining the properties of nanostructure structures [42].

In this thesis, InGaN/GaN MQWs were successfully grown on nonpolar structure. A-plane and c-plane MQWs with the same growth condition were prepared to be compared in their optical characteristic. The presence of obvious power-depend blue-shift on PL peak was observed for c-plane MQWs, whereas less shift was observed for a-plane MQWs. Furthermore the superlinear relation between excitation power and luminance intensity was studied. The direct proportion relation was shown in the result of a-plane MQWs, but superlinear was relation shown in that of c-plane QWs. The superlinear relation can be recognized that the nonradiative process

resulting from built-in electric field is screen by photon injected carriers. However, in a-plane MQWs, the polarization does not affect in the direction of well resulting in direct proportion relation.

On the other hand, in InGaN system, exciton localization phenomenon was a unique characteristic [43-44]. The low miscibility between InN and GaN or phase separation leads to spatial In segregation. The potential fluctuation result in localized state which would trap carrier and help to enhance luminance efficiency. In section 5.2, we investigate the localization effect on a-plane InGaN MQW using temperature dependent PL and PLE. Low temperature PL spectrum exhibited two dominant peaks in a-plane MQW. The apparent thermal quenching on high energy peak, whereas the luminance of low energy one maintain even until room temperature. And the lager stoke shift in a-plane MQW than c-plane MQW was addressed by PLE measurement. Those phenomenon demonstrated that the localization effect obviously appear in a-plane InGaN MQW.

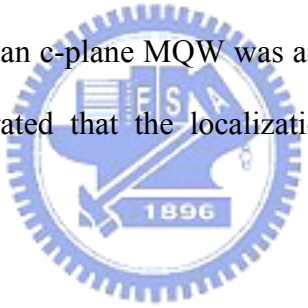

5.2 Polarization effects of c-plane and a-plane InGaN MQW

5.2.1 Sample preparation

The 5-period GaN/InGaN MQW samples were simultaneously grown on a-plane GaN/r-plane sapphire and c-plane GaN/c-plane sapphire template layers in metal-organic chemical vapor deposition (MOCVD) reactor. Trimethylgallium, ammonia and disilane were the precursors used to GaN growth. The buffer layer was grown at 550˚C and the epilayer was grown at 1050˚C. After the deposition of GaN template structure InGaN MQWs were grown at 856˚C and 845˚C for two sets of samples. We took two sets of samples (A1, C1 and A2, C2) to compare their optical properties. Samples A1 and C1 are MQWs deposited on a-plane and c-plane GaN template at 856˚C. And A2 and C2 were grown on the other equitant condition 845˚C.

5.2.2 Room temperature photoluminescence spectra

The optical characteristic of the a-plane InGaN/GaN MQW samples were evaluated with a 24mW He-Cd laser operated at 325nm. The laser beam was collimated to a spot of 100um in diameter. Figure 5.2.1 shows the corresponding PL spectra at room temperature for each one. The dominant peak energy (wavelength) for sample A1, C1, A2, C2 is 3.089 eV (401nm), 3.153 eV (393nm), 3.028 eV (410nm) and 3.058 eV (405nm), respectively. The PL peak of those samples and growth temperature are listed in Table 5.2.1. PL spectra show the lower growth temperature, the longer PL peak wavelength. The reason was In tend to thermally diffuses out in higher growth temperature. The PL intensity of a-plane samples were one order magnitude lower compared with c-plane samples. In the PL spectra, the weaker PL intensity of sample A1 in compare of other c-plane samples reveals the presence of GaN emission at 3.4 eV. A-plane MQW exhibited lower intensity and broader half of full width. Furthermore yellow band emission was observed especially for a-plane MQWs. Those behaviors can be explained related to high density of structure defects and surface roughness [45]. In Figure 5.2.3 dislocations on sample A1 are seen as sharp-triangular lines propagating parallel to the substrate. These pits are the general from of V defects, which are observed in c-plane InGaN alloy customtly. For a c-plane film, the V defect is an open, inverted pyramid bound by the pyramidal $[10\bar{1}0]$ facets. In the nonpolar orientation, V defect appears as a < defect.

5.2.3 Power dependent photoluminescence

In order to observe the influence of built-in electric field on a-plane and c-plane MQW, the power dependent PL measurement was demonstrated. Figure 5.2.4 shows RT PL spectra for sample C2 as shown in Figure 5.2.4 (a) and sample A2 as shown in Fig. 5.2.4 (b) of InGaN/GaN MQW from 32uw to 22mW. The PL peaks of sample C2

undergo a clear blue shift with increasing power density. But PL peaks of sample A2 exhibit less dependence on excitation power density. The power dependent PL peak shifts from 1.63 W/cm^2 to 293W/cm^2 are shown in Fig. 5.2.5. The total shifts of four samples are about 5.5 meV, 13.2 meV, 7.49 meV and 33.02 meV for A1, C1, A2 and C2, respectively. C-plane samples with obviously blue shifts are attributed to the presence of larger built in electric field as the best-known. In particular, a-plane samples show a little blue shift indicates the reducing built-in field existing in a-plane samples, e.g. growing along nonpolar direction and less influenced by internal polarization. The larger shifts in C2 than C1 and A2 than A1 are due to larger strain-influenced internal field. It is prospered that larger strain inducing field resulted from higher In composition. In addition, the excitation power dependence on luminance intensity is analyzed by room temperature dependent PL. Figure 5.2.6 shows the relation between excitation power and luminance intensity for both A2 and C2. In the case of c-plane MQWs, the superlinear relation ($I \sim P^{1.446}$) is demonstrated; whereas in the case of a-plane sample, the luminance intensity increase linearly with power density ($I \sim P^{1.078}$). The superlinear relation is due to decreasing nonrecombination process screen with photo-injected carriers. In other words, the total internal field is reduced by accumulating carriers in one side of triangular potential when we increase excitation power density which is well know as screen effect. Therefore, it can be concluded that nonrecombination resulted from QCSE play a minor role in nonpolar structure.

5.3 Investigation of localization effect in a-plane MQW

5.3.1 Low temperature and temperature dependent photoluminescence

To further study the emphasis of localization effect on our samples, temperature dependent PL was applied. The low temperature PL spectra of four samples at 20k are

shown in Fig 5.3.1. The spectra show two separated peaks for a-plane MQWs obviously. Two peaks for A1 and A2 are at 3.189, 3.295 and 3.138, 3.246, respectively. The observation of separated two peaks is suggested due to localized tail states. Typically, so-called localized states originated from spatial In segregation. For III-V semiconductor, the recombination of localized exciton at the potential minima is responsible for the luminance mechanism. In InGaN alloy, the possible origin of the In rich disorder are likely due to the defect-resistance nature [46]. The defective structures consists V-defect structure with threading dislocation (TD). They are observed associated with In-rich cluster witch is responsible for the localization effect. The evidence and behavior of exciton localization in our investigation will be discussed later.

Fig 5.3.2 illustrates the temperature dependent PL spectra. At 20K, the two peaks reveal almost equal intensity. However, the high energy peak exhibits remarkable thermal quenching. After 160K, it hardly can be recognized, but lower energy peak dominate the luminance until room temperature. In general case, the temperature dependent quench in luminance can be explained by thermal emission of the carriers with activation energy out of the confining potential. Since activation of high energy peak is measured about 27meV and much less than the band offsets of conduction or/and valance band, the thermal quenching effect is not resulted from the carriers run out of the well into barrier. Otherwise, the most possible reason related to the luminance mechanism is originated from potential fluctuation. The higher energy peak is suggested due to the localization state with deep potential. At low temperature, excitons are randomly trapped by the spatial localized state. As increasing temperature, the thermally activated excitons obtain energy then delocalizated. Finally, they can be trapped by the nonrecombination center during transfer or relax in deeper potential minima. As a result, the high energy peak experience fast quenching and low

energy peak contribute the dominant luminance at high temperature as we observed.

5.3.2 Photoluminescence Excitation

Photoluminescence excitation (PLE) can provide us the information of absorption spectrum and understand the distribution of energy state. Our PLE spectra along with PL measurement of four samples are shown in Fig.5.3.3. The measurements are carried out at 20K in order to get efficient luminance. The dispersed light comes from the monochrometer in front of a Xe lamp with continuous radiation. All of the PL spectra are measured by the excitation of dispersed light at 325nm come from Xe lamp. Acquire for the quantitative comparison, all of the PLE spectra are normalized to unity at their maximum. In order to analyze the Stokes' shift defined as the difference in energy between the effective band gap and the emission peak energy, it is essential to have an accurate description of the absorption edge that includes the effects of broadening. A PLE measurement was performed to get the absorption edge, Martin *et al.* suggested that by fitting the PLE spectra to the sigmoidal formula

$$\mathrm{I}(E) = \frac{\mathrm{I}_0}{1+\exp(\frac{E_{eff}-E}{\Delta E})} \qquad \text{Eq. (5.2.2)}$$

where I_0 is the maximum intensity, Eeff is the effectve band gap, ΔE is the boarding factor which is related the distribution of absorption state. In Fig 5.3.3, a sharp peak for each sample at about 3.49eV is the signal from GaN barrier, clearly seen for all the PLE spectra. As can be seen at low temperature PL spectra exciting by He-Cd laser, two separated peaks also presented at the excitation of Xe lamp. Now we focus on the low energy peak because it dominant in the luminance mechanism from 20K to 300K. The experimental and fitting results are list in table 5.3.1. The stoke shift of A1, C1, A2 and C2 are 236, 341, 224 and 275meV, respectively. The Stokes shift in the InGaN QW is resulted from the separation of wavefunction overlap due to the built-in

internal field and the presence of localized states [47-48]. From the above observation, the power dependent experiments indicate the influence on built-in internal field can be neglected in a-plane QW. Furthermore, in the same growth condition, the observations show that a-plane sample exhibited larger stokes shift than c-plane sample. This phenomenon indicates obvious localization effect in a-plane samples and the result may be corresponding to the behavior of defect associated with In rich disordered clusters reported for polar [0001] InGaN/GaN QWs [46].

5.4 Conclusion

In conclusion, the optical properties on polarization effect of a-plane InGaN/GaN MQWs and c-plane MQWs were investigated. Compare with c-plane MQWs, a-plane MQWs exhibited less power dependent blue shift due to not effected by quantum confine stark effect (QCSE). Moreover, the power dependent luminance intensity was demonstrated, too. The superlinear relation ($I \sim P^{1.446}$) of c-plane MQWs revealed the recombination efficiency increase by gradually screen of the bending potential. But the proportion relation ($I \sim P^{1.078}$) in a-plane sample indicated the flat band structure witch agrees with the absence of the build in field along the direction of QWs.

Finally, the localization effect of a-plane MQWs was investigated by temperature dependent PL and PLE experiment. We observed two separated peaks at 20k in a-plane sample; whereas only one peak in c-plane sample. In a-plane sample, high energy peak experience dramatic thermal quenching but low energy peak kept the luminance until room temperature. This temperature dependent experiment indicated the low energy peak result from the localization state with stable luminance efficiency. Analysis of PLE experience show the apparent stoke shift also conclude the obvious localization in a-plane MQWs.

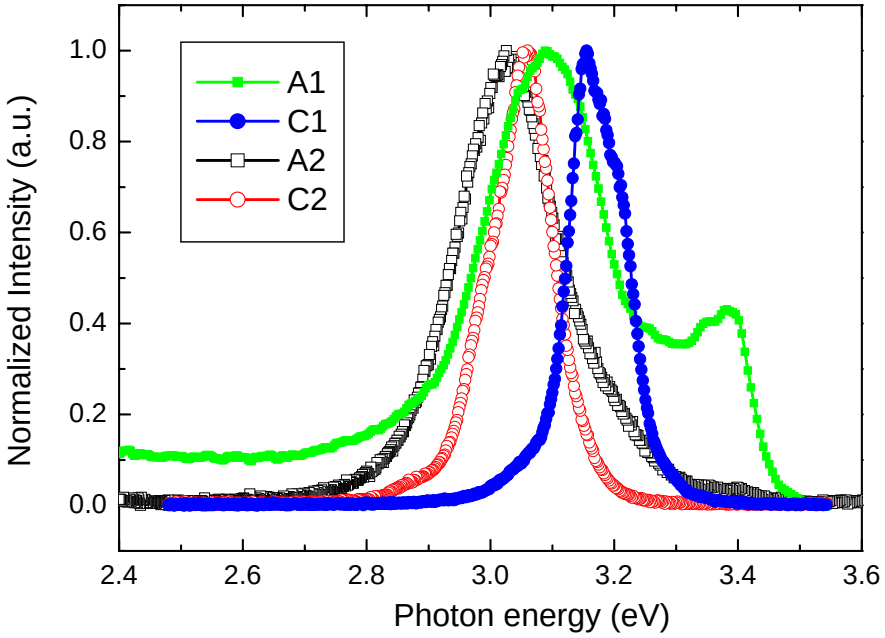

Fig. 5.2.1 Room temperature PL of sample A1,C1,A2 and C2

	PL peak	Growth T
A1	3.089 eV	856 ˚C
C1	3.153 eV	
A2	3.028 eV	845 ˚C
C2	3.058 eV	

Table 5.2.1 List of PL peaks and the growth temperature

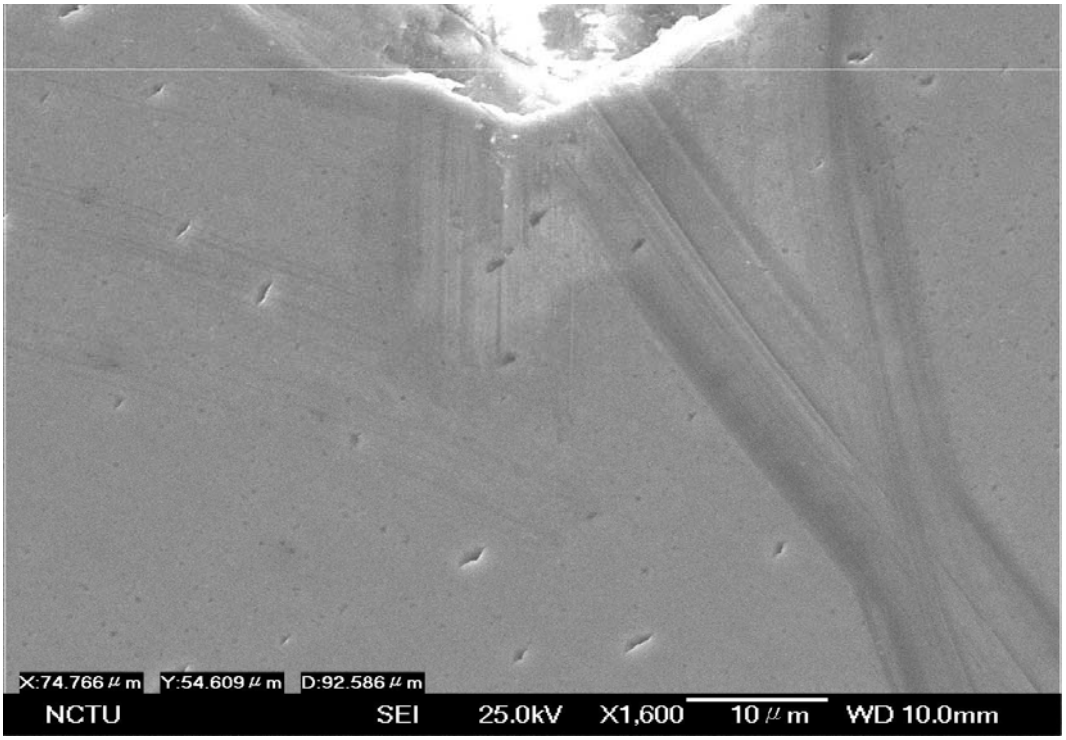

Fig. 5.2.2 : SEM image of sample A1

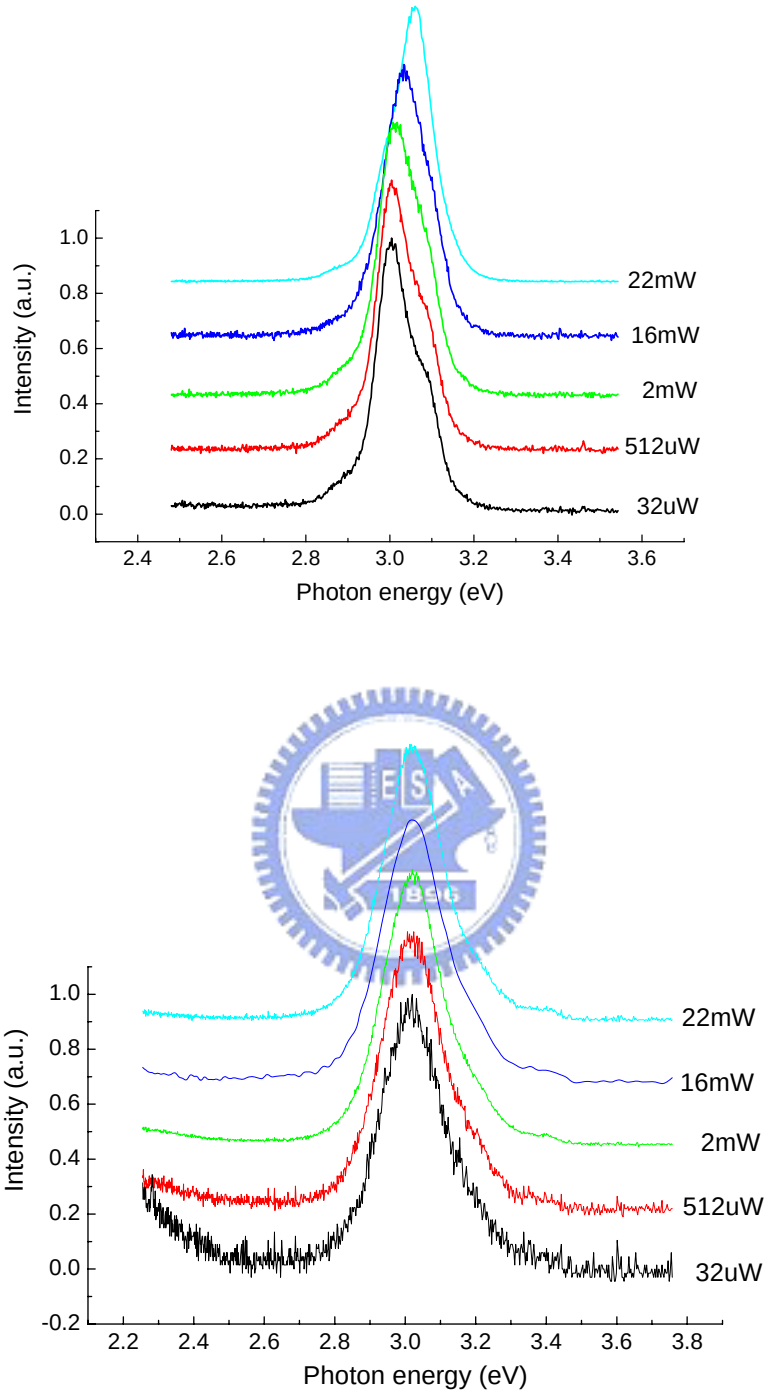

Fig. 5.2.3 Excitation power dependent PL of (a) sample C2 and (b) sample A2

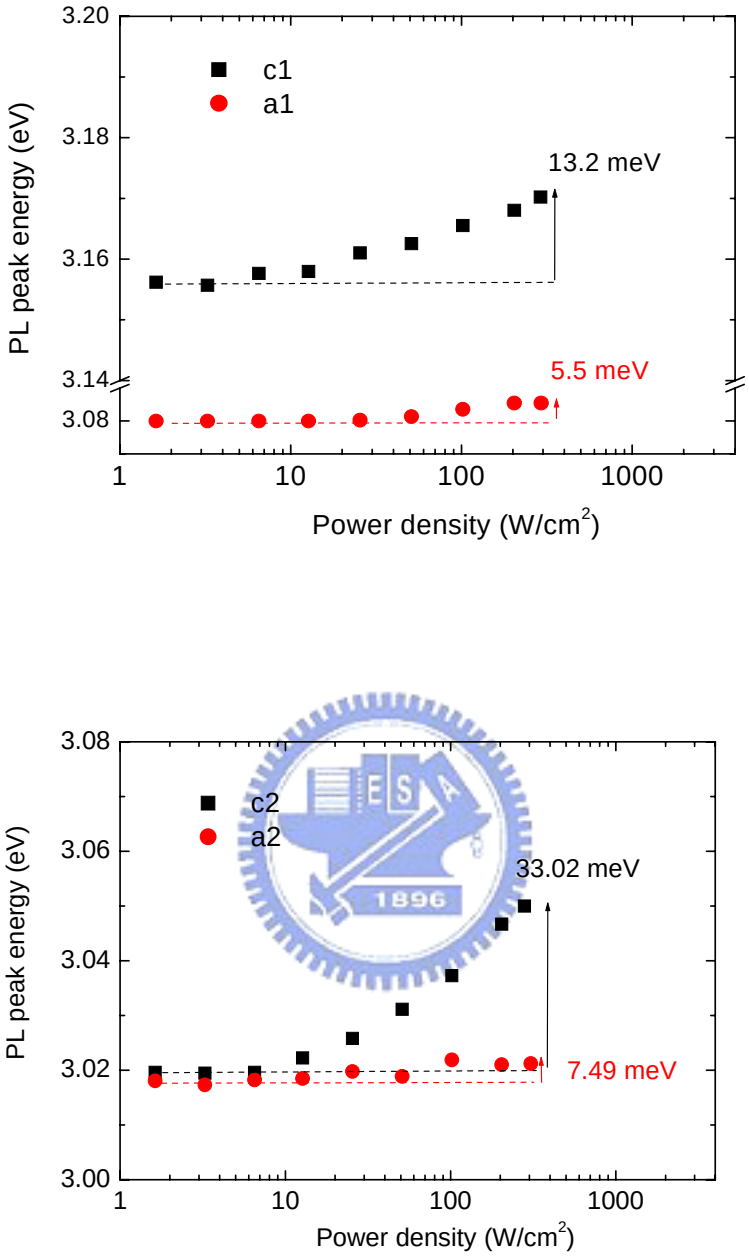

Fig. 5.2.4 Dependence of peak energy of the PL spectrum on excitation power density (a) A1/C1 and (b) A2/C2

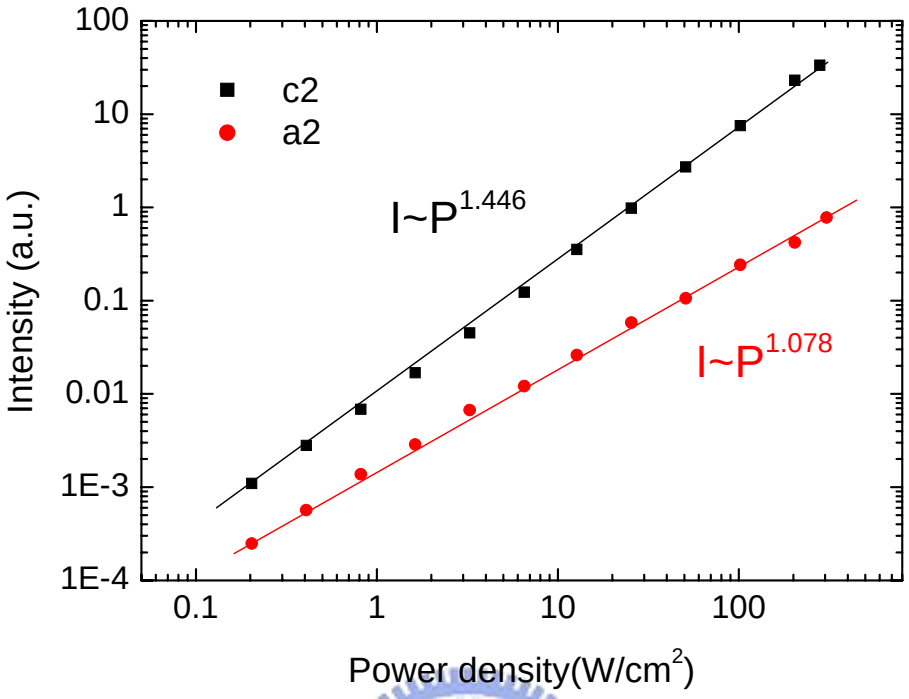

Fig. 5.2.5 PL intensity dependence on excitation power density of a-plane(A2) and c-plane sample(C2)

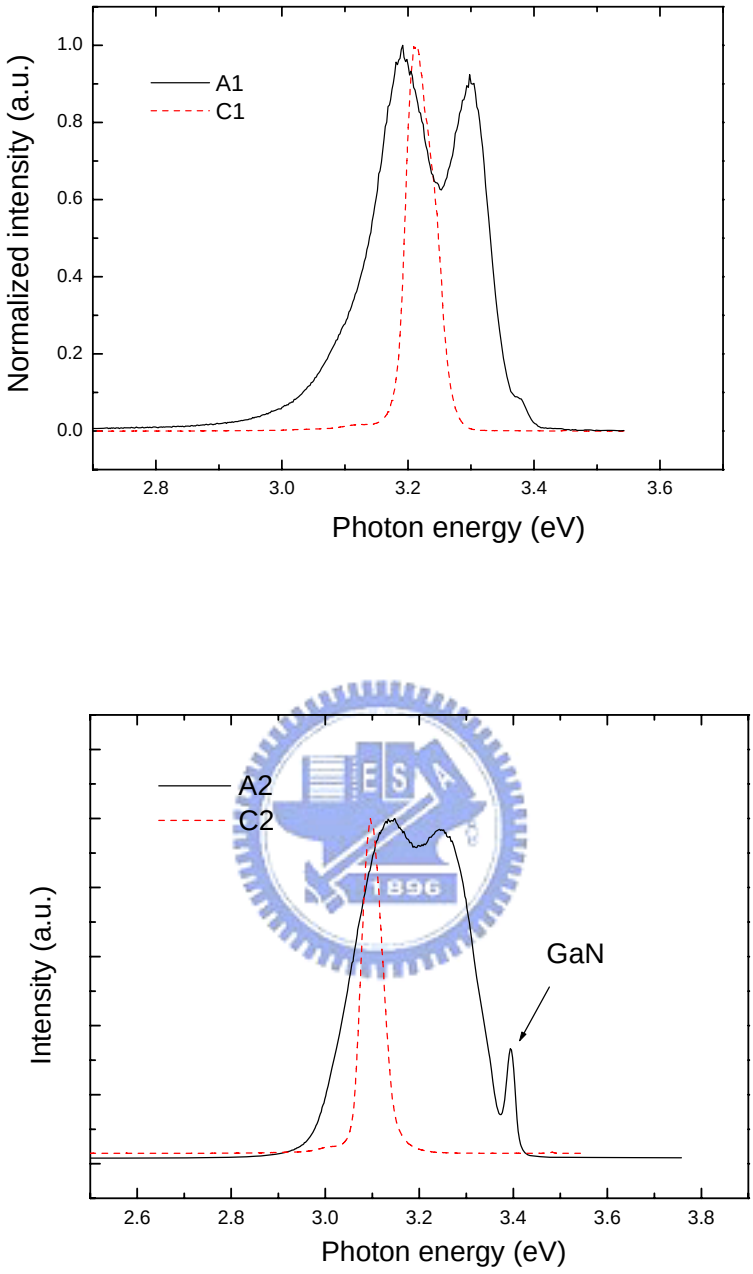

Fig. 5.3.1 Low temperature PL spectrum at 20 K (a) A1/C1 (b) A2/C2

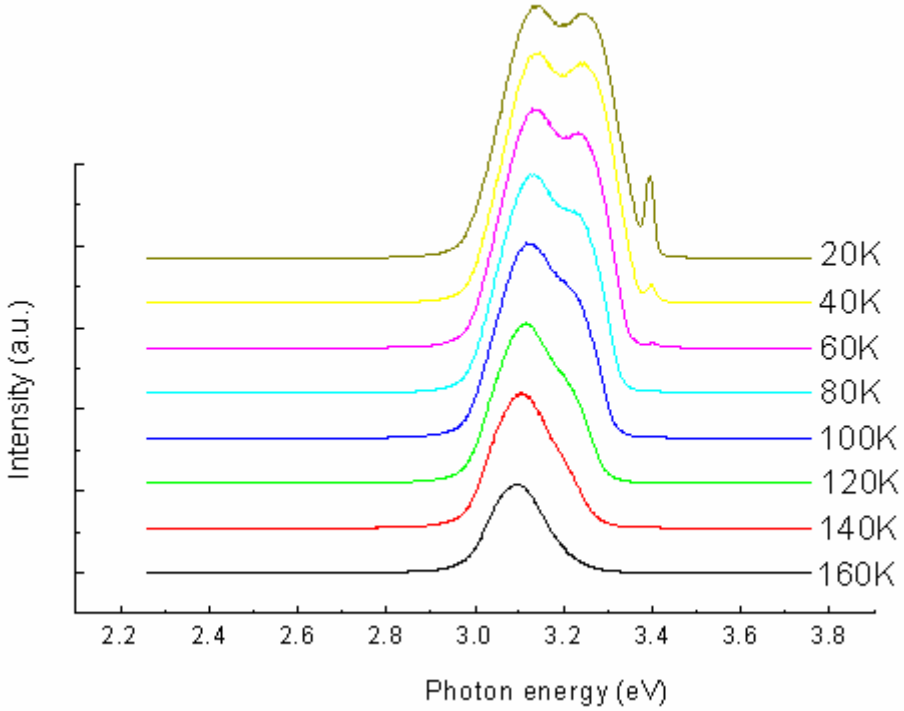

Fig. 5.3.2 Temperature dependence PL spectrum at 20 K

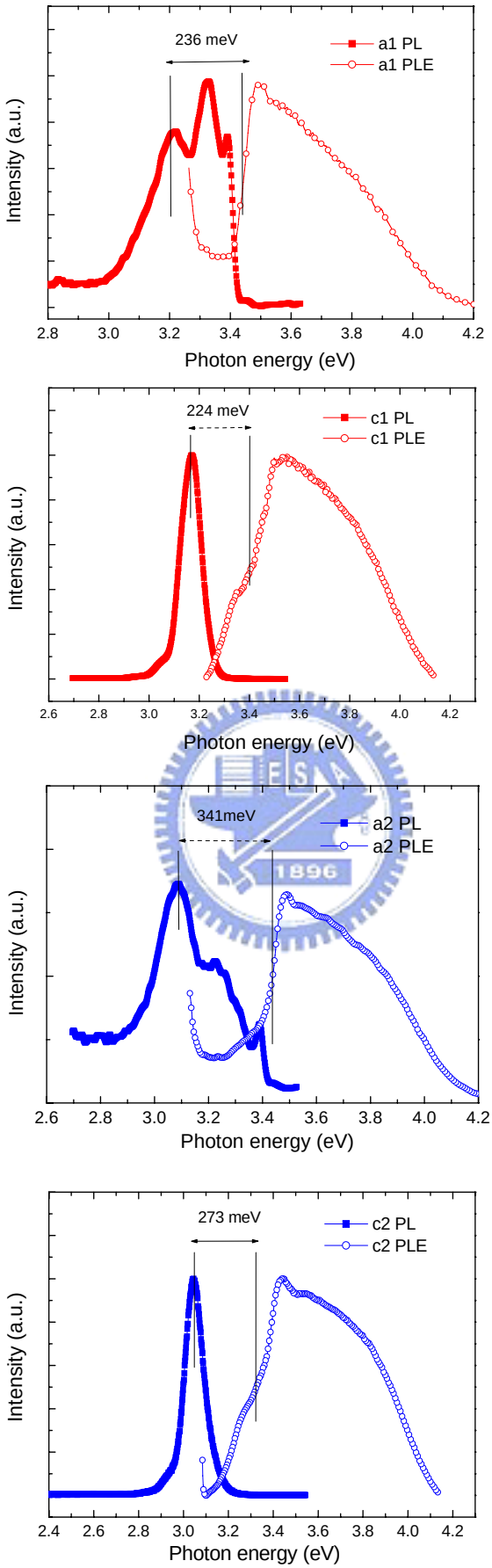

Fig 5.3.3 PL and PLE spectra of a-plane and c-plane InGaN/GaN MQWs

	PL peak (eV)	Eg (eV)	Stoke shift (meV)	△E (meV)
A1	3.210	3.446	236	14
A2	3.088	3.429	341	33
C1	3.168	3.392	224	61
C2	3.036	3.311	275	65

Table 5.3.1 Experimental and fitting factors of PLE measurement of a-plane and c-plane InGaN/GaN MQWs

Chapter 6 Trenched laterally over-grown *a*-plane GaN with low dislocations density

6.1 Introduction

The quantum efficiency of light emitting diodes (LEDs) and laser diodes (LDs) based on group-III nitride heterostructures is reduced due to the presence of built-in electric fields. The polarization-related electric fields contributed by the spontaneous and piezoelectric polarizations cause electron and hole separation in quantum wells that lead to inclining of band structure, poor recombination efficiencies, reduced oscillator strength, and red shift in emission wavelength. The spontaneous and piezoelectric polarizations paralleled to [0001] *c* direction of GaN based devices are caused by the arrangement of atoms and strain in MQW, respectively. As a result, the performances of III-nitride devices are limited by the polarization-related internal electric fields.

Without polarization effects, non-polar GaN is currently the subject of intense research due to the potential to improve the internal quantum efficiency (IQE) of GaN optoelectronic devices. To eliminate such polarization effects, growth along nonpolar orientations has been respectively explored for $[11\bar{2}0]$ *a*-plane GaN on $[10\bar{1}2]$ *r*-plane sapphire [49] and *a*-plane SiC, [50] and $[10\bar{1}0]$ *m*-plane GaN on [100] $LiAlO_2$ substrates [51-52]. According to the recent studies of *a*-plane and *m*-plane AlInGaN based quantum wells demonstrate that it is possible to avoid such polarization fields effect by growing device structures along these nonpolar orientations.

However, nonpolar *a*-plane GaN base material grown on *r*-plane sapphire substrates which always accompany with a wavy, stripe-like growth feature possess a large density of threading dislocations and stacking faults. It is as result of the serious

aniostropic in-plane strain between different crystal axis [13]. Recently, successful epitaxial lateral overgrowth (ELOG) of *a*-plane GaN on *r*-plane sapphire has been reported. ELOG not only improves significantly the material quality by reducing the density of threading dislocations but also alleviates the strain-related surface roughening and faceting [14]. Despite the ELOG assisted morphology and quality improvements in *a*-plane GaN over *r*-plane sapphire, the study of the epilayer quality and dislocations distribution in the ELOG epilayer is quite not lucid. In this letter, we successfully improve $[11\bar{2}0]$ *a*-plane GaN quality by using TELOG and the optical and structural properties is presented explicitly.

6.2 Sample preparation

Fig.6.2.1 shows the flow chart of the process sequence of the *a-GaN* template and subsequent TELOG. At first, the *a*-plane GaN templates with 1.5μm thickness were grown with low pressure-metalorganic vapor phase epitaxy (LP-MOVPE) on *r*-plane Al_2O_3 substrates using conventional two-step growth technique. After a serial of conventional photolithography techniques, a 2 μm/18 μm (window/wing) TELOG stripe pattern orientation was chosen parallel to the $[1\bar{1}00]$ direction to realize vertical *c*-plane sidewalls. Mask patterning was followed by etching of SiO_2 using inductively coupled plasma etching through the windows to the GaN epitaxial film. GaN stripes were etching through the mask openings, down to the *r*-plane sapphire substrate, thus forming Ga-face [0001] and N-face $[000\bar{1}]$ planes on the sidewalls and exposed *r*-plane sapphire at the bottom of the trenches by reactive ion etching. To simplify the growth process, the SiO_2 mask was removed by hydrofluoric acid and followed by depositing *a*-plane GaN TELOG film using single-step growth process. The growth condition in this study were described as follow: growth temperature

~1190^{o}C low pressure and low V/III ratio, ~700-800.

6.3 SEM image

To observe the growth behavior and mechanism, we stop the process before coalescence. As shown in Fig.6.3.1, the Cross-sectional SEM images of TELOG by MOCVD, the Ga-face growth rate was faster than N-face growth rate with a thin GaN layer about 0.2μm grown on the bottom of the trenches. The thin GaN layer will influence the quality and growth of TELOG. Furthermore, the influence by the thin GaN layer to Ga-face is more obvious than N-face so that the ratio of Ga-face growth rate / N-face growth rate is about twice, not as high as the reports of UCSB, an order of magnitude [15].

6.4 High-resolution X-Ray measurement

High-resolution X-Ray rocking curves, as shown in Fig.6.4.1, revealed that the *a*-plane GaN templates posses a serious anisotropic structural characteristics: the FWHM of as-grown *a*-GaN 1.5 μm bulk layer in $[1\bar{1}00]$ direction is almost twice as large as that in [0001] direction. It shows that the strains between the different crystal axis, for instance c-axis and m-axis, are quite different and enhance the formation of line defect. Moreover, the surface geometry becomes a wavy, stripe-like growth feature while the nucleation layer was not optimized or the thickness is thicker and thicker as result of some pits on the thin film. However, after lateral overgrowth, the stresses of TELOG layer were released in both c-axis and m-axis and thus the crystal quality was enhanced especially in the $[1\bar{1}00]$ direction so that the FWHM was reduced from 1810 arcsec to 351 arcsec. On the other hand, since the strip of the TELOG layer did not coalesce, we observed obvious wing tilt phenomenon along

[0001] direction which leads to the X-Ray rocking curve broadening effect. Unlike the symmetric wing tilt in *c*-plane TELOG GaN [53-54], the wing tilt in *a*-plane TELOG GaN is asymmetric so that the X-Ray rocking curve shows the asymmetric profile. This results in asymmetric overgrown wings [55] which possess the different lateral growth rates of the window GaN in the [0001] and the $[000\bar{1}]$ directions. Although the FWHM was only reduced from 973 arcsec to 816 arcsec, the quality would be better while the TELOG film fully coalesced and without wing tilt phenomenon.

6.5 Micro-photoluminescence measurement

This phenomenon was confirmed by micro-photoluminescence (μ-PL) of *a*-plane TELOG. We use a scanning near-field optical microscope (SNOM) to scan a 25 μm×25 μm confocal image. The sample is excited by a He-Cd laser operating on 325 nm with 25 mW. Using a 40×objective, He-Cd laser is focused into a spot with 1 μm in diameter on sample. The photoluminescence is collected in a fiber with 25 μm in the diameter and detected by a Photo Multiplier Tube (PMT). Furthermore, μ-PL spectra is dispersed by a 320mm monochromator (Jobin-Yvon Triax 320). The wavelength resolution is about 1nm by using 300 grooves/mm grating and the slit of 0.1 mm. Although the Fabry-Perot effect make the multi peaks be found in the μ-PL spectra, we still can ascertain the quality of GaN by the μ-PL intensity. As shown in Fig.6.5.1, five different regions were easily distinguished in the TELOG sample. Comparing the μ-PL data with SEM image, the stripped *a*-GaN seed stands at region 2 and the best crystal quality area, region 1, the strongest μ-PL intensity area, stands at the N-face GaN wing. On the contrary, the worst crystal quality area, region 5, the lowest u-PL intensity area, stands at the un-coalesced widows region so that *a*-GaN

can grow on r-sapphire without nucleation layer but has a very texture surface and not thicker than 0.3 μm as Fig. 2 shows. Another good quality area, region 3, stands at the initial region of the Ga-face GaN Wing, region 4. We suggest that the crystal quality of Ga-face GaN possesses higher growth rate easily is effected by the thin *a*-GaN layer grown in the un-coalesced windows but not obviously at the beginning of re-growth while the thin *a*-GaN layer was not formed.

6.6 Cross-sectional transmission electron microscopy (TEM) measurement

The distributions and types of dislocations were investigated by cross-sectional transmission electron microscopy (TEM) shown as Fig.6.6.1. According to the g=($11\bar{2}0$) and g=(0002) two beam bright field images, most of the threading dislocations are in contrast in both of the g=($11\bar{2}0$) and (0002) two beam condition, indicating that these dislocations are mixed a+c type dislocations. The distribution of dislocations fully consists with the u-PL results. The threading dislocations densities (TDD) of stripped GaN seed were more than 1×10^{10} cm^{-2}. TDD of Ga-face GaN wing which was influenced by the thin layer is about 3×10^{8} cm^{-2} and TDD of N-face GaN wing about 3×10^{7} cm^{-2}, three orders of magnitude lower than planar films, is not influenced as obviously as Ga-face GaN wing. This is a stronger evidence to support the suggestion that Ga-face GaN is easier to overgrowth and is influenced by the thin GaN layer on the bottom of trench. As a result, a better quality *a*-plane TELOG GaN can be established on a pattern into the sapphire surface over 0.3 μm depth.

6.7 Cathodoluminescence (CL) image

To realize the relationship of optical property and TDD, the Cross-sectional Cathodoluminescence (CL) image of *a*-plane TELOG was photographed, shown as

Fig.6.7.1. The CL intensity distribution is almost the same as the results investigated by TEM. So that the dislocations still perform as the non-radiative center in *a*-plane GaN film and become the principle problem what should be solved immediately. According the above results, we perform the same process with a 3 μm/7 μm stripe pattern, shown as the Fig.6.7.2. The coalescence process can fully be completed below 10μm, it is a useful technique to overcome the thickness problem that ELOG always need more than 30μm to fully coalescence. The FWHM of X-Ray can be reduced to 385arcsec in [0001] and 260arcsec in $[1\bar{1}00]$ direction without wing tilt phenomenon.

6.8 Cnclusion

In conclusion, the quality of *a*-plane GaN film was successfully improved by using TELOG and the TDD can be reduced. Meanwhile the phenomenon of anisotropic in-plane strain between different crystal axis also can be mitigated by TELOG. Furthermore, the best quality area stands at the N-face GaN wing. The Ga-face GaN is easier to overgrowth and is influenced by the thin GaN layer on the bottom of trench. According the results of PL, TEM, and CL, the threading dislocations are the mainly non-radiative center in *a*-plane GaN film. Finally, we conclude that a narrower stripped GaN seeds and deeper stripped patterns etched into the surface of sapphire can derive a better quality *a*-plane TELOG GaN film and the all coalescence process can be finished below 10μm thick.

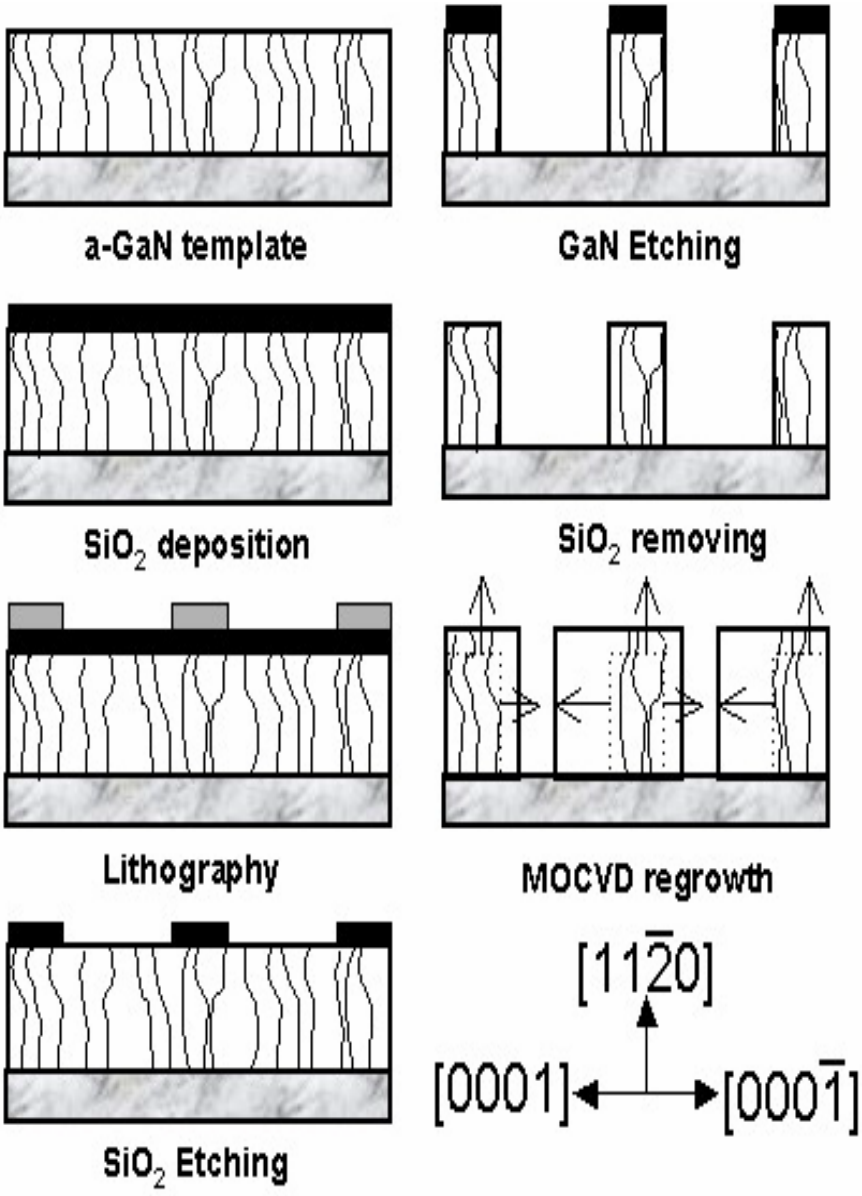

Fig.6.2.1 Flow chart of *a*-plane GaN TELOG process

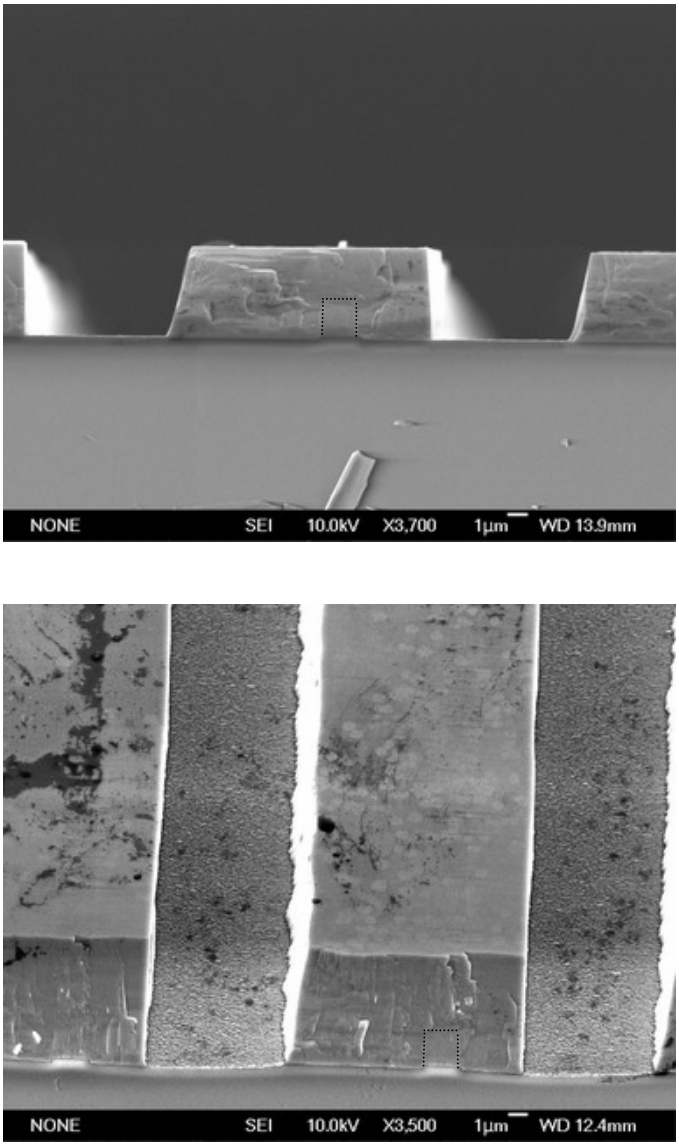

Fig.6.3.1 Cross-sectional SEM of *a*-plane GaN TELOG

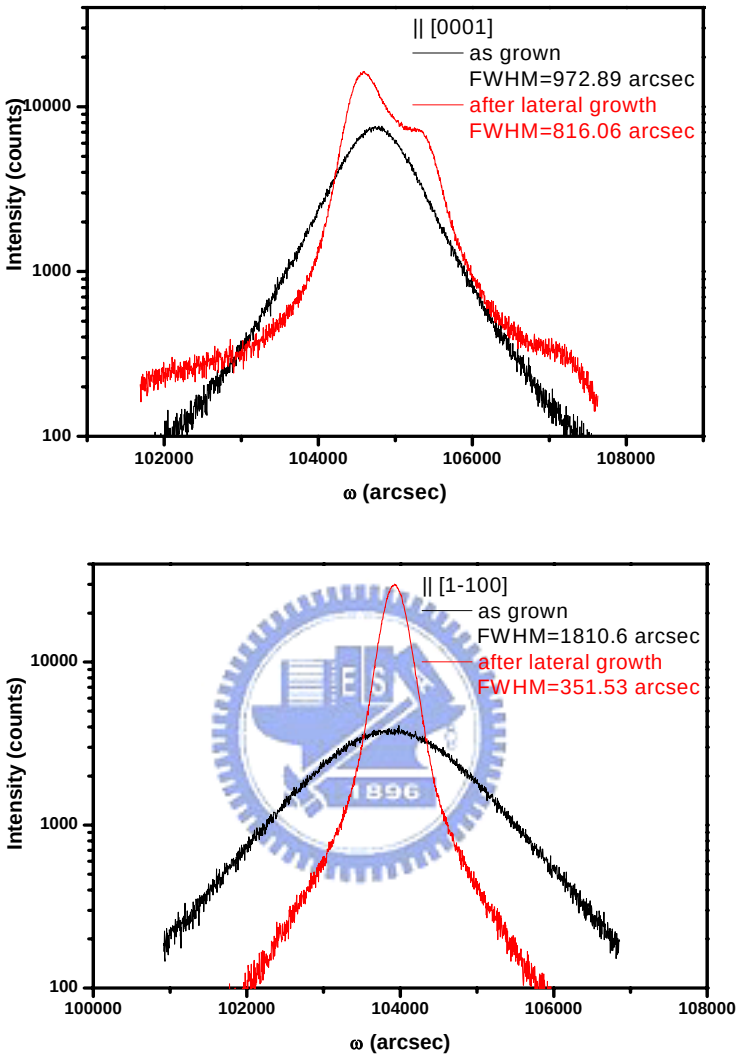

Fig.6.4.1 X-Ray rocking of *a*-plane GaN TELOG

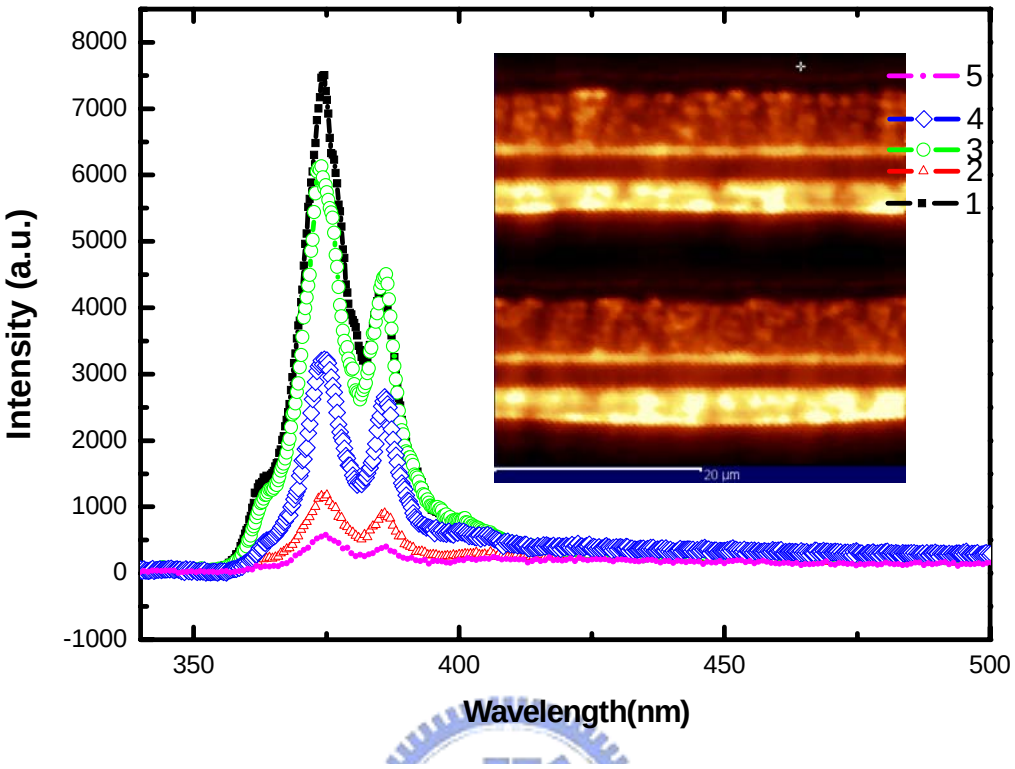

Fig.6.5.1 μ-PL of *a*-plane GaN

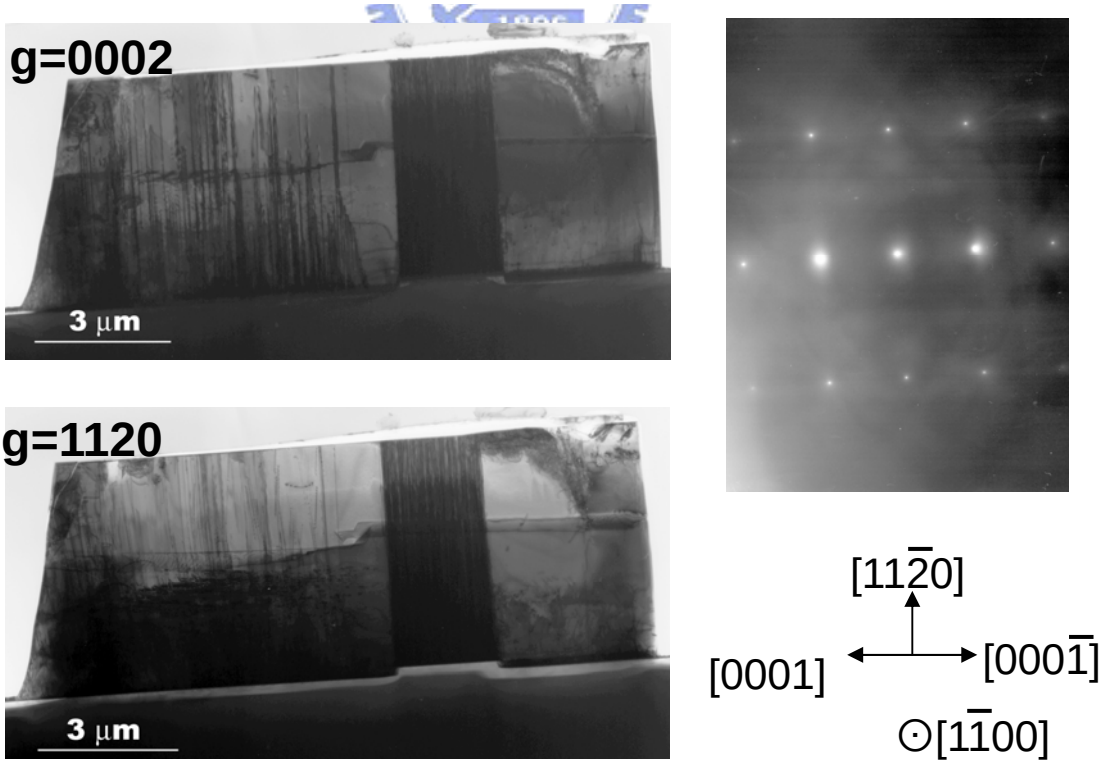

Fig.6.6.1 Cross-sectional TEM image of *a*-plane GaN TELOG

Fig.6.7.1Cross-sectional CL image of *a*-plane GaN TELOG

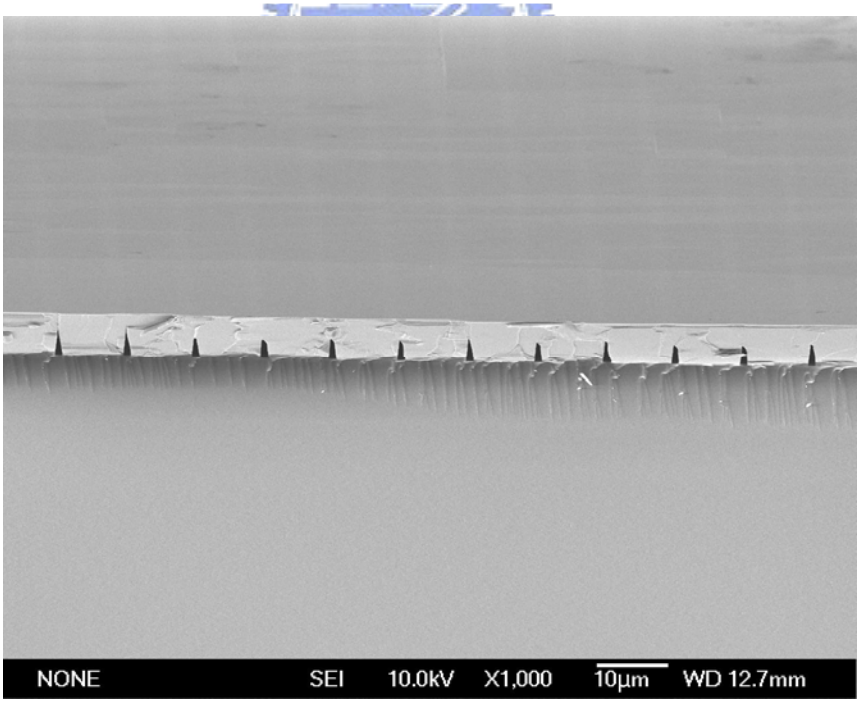

Fig.6.7.2 Cross-sectional SEM of *a*-plane GaN 3 μm/7 μm TELOG

Chapter 7 Conclusion and future work

7.1 Conclusion

We have studied the structure and optical characteristic for two kinds of nanostructure. The first part is InGaN/GaN quantum dots (QDs) and the second part is a-plane InGaN/GaN multiple quantum wells (QWs) on r-plane sapphire. The conclusions are demonstrated as follows:

First, we have showed a new way to grow the InGaN QDs of different sizes on SiN_x nanohole. With increasing SiN_x duration time, we obtain larger size of QDs. The PL peak energy was decrease with increasing the QD size due to reduction of quantum confine. The simulation of transition energies are agreed with the PL measurement. On the other hand, we have investigated effects of thermal annealing on the optical properties of InGaN/GaN QDs by PL measurement and theoretical simulation. A red-shift followed by a blue-shift of PL peaks of InGaN QDs was observed as increasing the annealing temperature. We also provide a theoretical simulation to analyze the mechanism of the InGaN/GaN QDs of thermal annealing. The results indicate that the variations of transition energies were contributed to the QD size enlargement and barrier height reduction. The former contributed to a red-shift and the later contributed to a blue-shift on the emission peak energy. Finally, temperature dependent PL experiments further supported that thermal annealing would increase QD size and decrease potential depth in the QD.

Second, the optical properties on polarization effect of a-plane InGaN/GaN MQWs and c-plane MQWs were investigated. Compare with c-plane MQWs, a-plane MQWs exhibited less power dependent blue shift due to not effected by the polarization effect. Moreover, the power dependent luminance intensity was demonstrated, too. The superlinear relation ($I \sim P^{1.446}$) of c-plane MQWs revealed the recombination efficiency increase by gradually screen of the bending potential. But

the proportion relation ($I \sim P^{1.078}$) in a-plane sample indicated the flat band structure witch agrees with the absence of the build in field along the direction of QWs. In addition, the localization effect of a-plane MQWs was investigated by temperature dependent PL and PLE experiment. We observed two separated peaks at 20k in a-plane sample; whereas only one peak in c-plane sample. In a-plane sample, high energy peak experience dramatic thermal quenching but low energy peak kept the luminance until room temperature. This temperature dependent experiment indicated the low energy peak result from the localization state with stable luminance efficiency. Analysis of PLE experience show the apparent stoke's shift also conclude the obvious localization in a-plane MQWs.. Finally, The trenched lateral epitaxial overgrowth (TELOG) GaN structure was introduced to overcome the high defect density. The Ga-face GaN wing which was influenced by the thin layer is about 3×10^{8} cm^{-2} and TDD of N-face GaN wing about 3×10^{7} cm^{-2}, three orders of magnitude lower than planar films TLEO method was developed successfully and reduce the defect density.

7.2 Future work

Although we have successfully developed nonpolar structures and measured the optical characteristics. The defective structure due to the asymmetric strain is hardly overcome on the template a-plane GaN on r-plane sapphire. We hope TLEO method can be applied in the growth of MQWs in the future.

Reference

[1] U. Woggon, *Optical Properties of Semiconductor Quantum Dots* (Springer, Berlin, 1997)

[2] J. K. Sheu, Y. K. Su, G. C. Chi, P. L. Koh, M. J. Jou, C. M. Chang, C. C. Liu, and W. C. Hung, *Appl. Phys. Lett.,* **74**, 2340 (1999)

[3] S. Nakamura, T. Mukai and M. Senoh, *Appl. Phys. Lett.*, **64**, 1687 (1994)

[4] T. Someya, R.Werner, A. Forchel, M. Catalano, R. Cingolani, Y. Arakawa, Science, **285**, 1905 (1999)

[5] C. C. Kao, Y. C. Peng, H. H. Yao, J. Y. Tsai, Y. H. Chang, J. T. Chu, H. W. Huang, T. T. Kao, T. C. Lu, H. C. Kuo, and S. C. Wang, *Appl Phys. Lett.*, **87**, 081105 (2005)

[6] T. Uenoyama, *Phys. Rev. B*, **51**, 10228 (1995)

[7] J. E. Northrup and J. Neugebauer, Phys. Rev. B, **53**, 10477 (1996)

[8] M. D. Craven, S. H. Lim, F. Wu, J. S. Speck, and S. P. DenBaars, *Appl. Phys. Lett.* **81**, 469 (2002)

[9] M. D. Craven, F. Wu, A. Chakraborty, B. Imer, U. K. Mishra, S. P. DenBaars, and J. S. Speck, *Appl. Phys. Lett.*, **84**, 1281 (2004)

[10] H. M. Ng, *Appl. Phys. Lett.,* **80**, 4369 (2002)

[11] Y. J. Sun, O. Brandt, M. Ramsteiner, H. T. Grahn, and K. H. Ploog, *Appl. Phys. Let,.* **82**, 3850 (2003)

[12] T. Onuma, A. Chakraborty, B. A. Haskell, S. Keller, S. P. DenBaars, J. S. Speck, S. Nakamura, and U. K. Mishra., *Appl. Phys. Lett.,* **86**, 151918 (2005)

[13] H. Wang, C. Chen, Z. Gong, J. Zhang, M. Gaevski, M. Su, J. Yang, and M. A. Khan, Appl. Phys. Lett. **84**. 499 (2004).

[14] M. D. Craven, S. H. Lim, F. Wu, J. S. Speck, and S. P. DenBaars, Appl. Phys. Lett. **81**, 1201 (2002).

[15] B. M. Imer, F. Wu, S. P. DenBaars, and J. S. Speck, Appl. Phys. Lett. **88**, 061908 (2006).

[16] S. Makino, T, Miyamoto, T. Kageyama, N. Nishyama, F. Koyama and K. Iga, *J. Cryst. Growth*, **221**,561 (2000)

[17] Satoru Tanaka, Sohachi Lwai, and Yoshinobu Aoyagi, *Appl. Phys. Lett.*, **69**, 4096 (1996)

[18] Xu-Qiang shen, Satoru Tanaka, Sohachi Lwai, and Yoshinobu Aoyagi, *Appl. Phys. Lett.*, **72**, 344 (1998)

[19] S. Sakai and T. Tatsumi, *Phys. Rev. Lett*, **71**, 4007 (1993)

[20] T. Takahashi and Y. Arakawa, *IEEE J. Quantum Electron*, 27, 1824 (1991)

[21] Peter Ramvall, Satoru Tanaka, Shintaro Nomura, Philippe Riblet, and Yoshinobu Aoyagi, *Appl. Phys. Lett.,* **73**, 1104 (1998)

[22] R. Melnik and M. Willatzen, *Nanotechnology*, **15**, 1 (2004)
[23] Ch.Manz, M.Kunzer and H.Obloh, *Appl. Phys. Lett.,* **74**, 3993 (1999).
[24] J. Wu, W. Walukiewicz, K. M. Yu, J. W. Ager III, E. E. Haller, H. Lu, and W. J. Schaff, *Appl. Phys. Lett .,* **80**, 4741 (2002).
[25] A. Cremades, V. Navarro, J. Piqueras, A. P. Lima, O. Ambacher, and M. Stutzmann, J. Appl. Phys. **90**, 4868 (2001)
[26] Feng Wu, Michael D. Craven,a) Sung-Hwan Lim, and James S. Speck, J. Appl. Phys. **94**, 942 (2003)
[27] E. Kuokstis,a) C. Q. Chen, M. E. Gaevski, W. H. Sun, J. W. Yang, G. Simin and M. Asif Khan, *Appl. Phys. Lett .,* **81**, 4130 (2002).
[28] Kittel, C., Wiley, New York, 1996
[29] Dingle, R., Sell, D.D., Stokowski, S.E. and Ilegems, M., *Phys. Rev B*, **4**,1211 (1971)
[30] Binnig, G., C. F. Quate, and C. Gerber, *phys. Rev. Lett.*,**56**,930 (1986)
[31] S. J. Pearton, J. C. Zolper, R. J. Shul, and F. Ren, *J. Appl. Phys.*, **86**, 1 (1999)
[32] J. K. Sheu, Y. K. Su, G. C. Chi, W. C. Chen, C. Y. Chen, C. N. Huang, J. M. Hong, Y. C. Yu, C. W. Wang, and E. K. Lin, J. Appl. Phys. **83**, 3172 (1998)
[33] S. Malik, C. Roberts, R. Murray, and M. Pate, *Appl. Phys. Lett.* **71**, 1987 (1997)
[34] M. G. Cheong, C. Liu, H. W. Choi, B. K. Lee, E. –K. Suh and H. J. Lee, *Appl. Phys. Lett.* **93**, 4691 (2003)
[35] J. F. Girard, C. Dion, P. Desjardins, C. Ni Allen, P. J. Poole, and S. Raymond, *Appl. Phys. Lett.*, **84**, 3382 (2004) [12] J. Crank, *Mathematics of Diffusion* (Clarendon, Oxford, 1957).
[36] C. C. Chuo, C. M. Lee, T,-E, Nee and J. I. Chyi, *Appl. Phys. Lett.*, **76**, 26 (2000)
[37] H. Fröhlich, *Proc. Soc. London,* **160**, 230 (1937)
[38] P. Ramvall, S. tanaka, S. Nomura, P, Riblet, and Y.Aoyagi, *Appl. Phys. Lett.,* **73**, 1104 (1998).
[39] P. Ramvall, S. tanaka, S. Nomura, P, Riblet, and Y.Aoyagi, *Appl. Phys. Lett.,* **75**, 1935 (1999).
[40] T.V. Torchynska, J.L. Casas Espinola, E. Vel_asquez Losada, P.G. Eliseev, A. Stintz, K.J. Malloy and Pena Sierra, *SURF SCI*, **532**, 848 (2003)
[41] Bernardini, V. Fiorentini, and D. Vanderbilt, *Phys. Rev. B*, **56**, R10024 (1997)
[42] E. Kuokstis, C. Q. Chen, M. E. Gaevski, W. H. Sun, J. W. Yang, G. Simin, and M. Asif Khan, *Appl. Phys. Lett.,* **81**, 4130 (2002)
[43] I. L. Krestnikov, N. N. Ledentsov, A. Hoffmann, D. Bimberg, A. V. Sakharov, W. V. Lundin, A. F. Tsatsul'nikov, A. S. Usikov, Z. I. Alferov, Y. G. Musikhin, and D. Gerthsen, *Phys. Rev. B*, **66**, 155310 (2002)
[44] R. Seguin, S. Rodt, A. Strittmatter, T. Bartel, A. Hoffmann, D. Bimberg, E. Hahn,

and D. Gerthsen, *Appl. Phys. Lett*. **84**, 4023 (2004)

[45] M. S. Jeong, Y. W. Kim, J. O. White, E.-K. Suh, M. G. Cheong, C. S. Kim, C.-H. Hong, and H. J. Lee, *Appl. Phys. Lett.,* **79**, 3440 (2001)

[46] D. I. Florescu, S. M. Ting, J. C. Ramer, D. S. Lee, V. N Merai, A. Parkeh, D. Lu, E. A. Armour and L. Chernyak, *Appl. Phys. Lett.,* **83**, 33 (2003)

[47] R. W. Martin, P. G. Middleton, and K. P. O'Donnell and W. Van der Stricht, *Appl. Phys. Lett.,* **74**, 263 (1999)

[48] Yong-Hoon Cho, B. J. Kwon, J. Barjon, J. Brault, B. Daudin, H. Mariette, and Le Si Dang, *Appl. Phys. Lett.,* **81**, 4934 (2002)

[49] M. D. Craven, S. H. Lim, F. Wu, J. S. Speck, and S. P. DenBaars, Appl. Phys. Lett. **81**, 469 (2002).

[50] M. D. Craven, A. Chakraborty, B. Imer, F. Wu, S. Keller, U. K. Mishra, J. S. Speck, and S. P. DenBaars, Phys. Status Solidi C **1**, 4 (2003).

[51] E. S. Hellman, Z. Liliental-Weber, and D. N. E. Buchanan, MRS Internet J. Nitride Semicond. Res. **2**, 30 (1997).

[52] P. Waltereit, O. Brandt, M. Ramsteiner, A. Trampert, H. T. Grahn, J. Menniger, M. Reiche, R. Uecker, P. Reiche, and K. H. Ploog, Phys. Status Solidi A **180**, 133 (2000).

[53] P. Fini, H. Marchand, J. P. Ibbetson, S. P. DenBaars, U. K. Mishra, and J. S. Speck, J. Cryst. Growth **209**, 581 (2000).

[54] W. M. Chen, P. J. McNally, K. Jacobs, T. Tuomi, A. N. Danilewsky, Z. R. Zytkiewicz, D. Lowney, J. Kanatharana, L. Knuuttila, and J. Riikonen, J. Cryst. Growth **243**, 94 (2002).

[55] C. Chen, J. Yang, H. Wang, J. Zhang, V. Adivarahan, M. Gaevski, E. Kuokstis, Z. Gong, M. Su, and M. Asif Khan, Jpn. J. Appl. Phys. **42**, L640 (2003).